Image Registration of Pulmonary SPECT and CT Exams

Lara Bolito Abrantes

Mestrado Integrado em Engenharia Biomédica

Setembro 2010

FCTUC

Image Registration of Pulmonary SPECT and CT Exams

Lara Bolito Abrantes

September 2010

Dissertation thesis to complete the necessary requirements to obtain the degree of Master in Biomedical Engineering

Qu'importa a fúria do mar.
Que a voz não te esmoreça vamos lutar.
José Afonso

Abstract

In the last years, medical imaging field has been had an enormous technological development. The application of 3D images extended its utility, becoming an essential tool to assist in the clinical diagnosis. There are several imaging modalities that allow to visualize different information about the body. In particular, with Computed Tomography (CT) anatomical information is obtained and with Single Photon Emission Computed Tomography (SPECT) the body metabolism is detected. By applying image processing methods it is possible to combine different visual information through multi-modality registration and consequently improve the clinical diagnosis.

In this thesis, a study of registration algorithms was done on 3D CT and SPECT images, in order to select the most appropriated transformation to identify bronchopulmonary segments with suspected pulmonary embolism. Rigid (rigid body, global rescale, specific rescale and affine) and non-rigid (diffeomorphic demons) transformations were applied. For each registration algorithm, processing time, image overlay and similarity measurements were analyzed. Affine transformation showed the best performance by allowing the combination of a good alignment and a low time to process. Therefore, it was considered the most suitable registration algorithm to identify suspected pathologic lung regions.

Acknowledgements

Many people help me during the last year on the execution of this Project. It was undoubtedly the cooperation and understanding of them who provided me the development and the achievement of this challenge Given the large number of people whom I want and I must express my gratitude, forgive me those who I could not mention however deserve all my respect for their dedication. Therefore, I would like to especially thank:

My advisor Professor José Silvestre Silva for his dedication, great support, rigor and discipline, attention, advising and transmitted knowledge.

My co-advisor Engineer Jorge Isidoro for all given support and contribution to this project.

To Electronics and Instrumentation Group (GEI) of Instrumentation Centre (CI) of FCTUC (Faculty of Sciences and Technology of the University of Coimbra) for having provided facilities, scientific equipment and logistical support for the implementation of work.

To Nuclear Medicine Service of the Coimbra University Hospitals, especially to Dr. Ana Paula Moreira, and other team member who directly or indirectly made possible the accomplishment of this work.

All my friends, for their unconditional support and encouragement in hard times and believing that I could carry out this goal. I cannot, however, fail to express my deepest gratitude to Ana Luísa Pinto, Ivânia Pereira, Catarina Pereira, Andrêa Gouvêa, Joana Caldas, Patrícia Matos and Catarina Bonito.

My collegues Fabiana Rodrigues, Sofia Antunes and Tiago Sapata for the friendship and enjoyable moments.

My uncle Adelino, for his patience and friendship that has always shown and for his morning rides.

My four-legged friends for the fellowship and the moments fulfilled of relaxation and fun.

Table of Contents

List of Figures

List of Tables

Glossary

CT	Computed Tomography
SPECT	Single Photon Emission Computed Tomography
PET	Positron Emission Tomography
MRI	Magnetic Resonance Imaging
PE	Pulmonary Embolism
RL	Right Lung
LL	Left Lung
2D	Two dimensional
3D	Three dimensional

1 | Introduction

This thesis reports the entire work developed within the ambit of the discipline of Project of Integrated Master in Biomedical Engineering, in a partnership between the Department of Physics of the Faculty of Sciences and Technology of the University of Coimbra and the Nuclear Medicine Service of the Coimbra University Hospitals.

1.1 | Motivation and Innovative Contribution

The pulmonary embolism occurs when a blood clot gets free from its origin place and travels through blood circulation until it reaches the lungs. As a consequence, the pulmonary artery, or one of its branches, is blocked. This type of pathology is more susceptible to occur in situations where the coagulation system is changed. Pulmonary embolism is difficult to diagnose due to its unspecified symptoms[1]. In Portugal, it is estimated an incidence of 25,000 cases of pulmonary embolism per year[2].

The application of imagiologic techniques has become an essential aid for the diagnosis of pulmonary embolism. As gold standard diagnosis, is used the pulmonary angiography. However, the development of the multislice Computed Tomography (CT) brought a high enhancement in image quality and the duration of the examination acquisition. Since CT examination only has anatomical information, the combination with metabolic information of Single Photon Emission Computed Tomography (SPECT) technique introduces an important improvement in the diagnosis of pathology[1] [3].

In this context, given the advantages of simultaneous use of images from different modalities in the diagnosis of pulmonary embolism, this study was developed. The main goals of this thesis are to analyze the behavior of the alignment of 3D CT and SPECT images and to identify lung regions with suspected pulmonary embolism.

Most of the works available in literature corresponds to the analysis of the lung as one piece, or using pulmonary lobes. This study goes to a deep level, identifying suspected pathologic bronchopulmonary segments. A comparison between several registration algorithms is performed in order to evaluate the most suitable methodology to be applied in context of identification of suspected pathologic regions.

In parallel of the execution of this project, an implementation and comparison of 3D multimodality registration was developed, which resulted in a publication in international conference [4].

1.2 | Structure of the thesis

This is thesis is organized according to the following structure. Chapter one reports the motivation and goals of the thesis and a summary to the contents of the remaining chapters.

In chapter two, it is given a few considerations about respiratory system, lung anatomy and pulmonary embolism disease that are useful to understand the developed study.

In chapter three, the imagiologic modalities of Computed Tomography and Single Positron Emission Computed Tomography are described, by focusing on the historical evolution of scanning system, the basic principles of image acquisition and the advantages and disadvantages of each modality.

In chapter four, image processing methods of segmentation and registration are defined and some relevant algorithms are exposed. A review of the literature is also presented with emphasis on the application of CT and SPECT images.

In chapter five, the applied methodology is presented, describing the pre processing steps, the segmentation and the registration method for the four cases analyzed suspected of pulmonary embolism.

In chapter six, the results are presented and discussed, by analyzing the accuracy of registration of the bronchopulmonary segments obtained from the segmentation process and the performance of the algorithms both in time and similarity metric value.

A summary of the discussion and results are written in the chapter seven, the conclusions. Proposals for further work are also presented.

2 | Lungs

In this chapter is described an overview of the anatomical and physiological characteristics of lungs and it is given a brief introduction to the Pulmonary Embolism disease.

2.1 | Anatomical and Physiological Considerations

The respiratory system transports the oxygen from air to the bloodstream during the inspiration and expels carbon dioxide from the blood through the expiration. Air enters into the body through the nose or mouth (Figure 1 (a)). After that, the air travels to the trachea by the larynx. The trachea is divided into two bronchi: one goes to the right lung and the other to the left lung. Successively, the bronchi are branched into bronchioles. At the end of the bronchioles are the alveoli. Each alveolus is covered with a small extension of the pulmonary arteries called capillaries. Thus, at the alveoli occurs the gases exchange (Figure 1 (b)). By diffusion the oxygen passes through the walls of the alveoli into the bloodstream. Afterwards, the oxygen that riches the blood travels to the heart through the pulmonary vein and its branches and by is delivered by the heart pumping to all the parts of our body. Simultaneously, the carbon dioxide travels in the opposite direction by crossing from the capillaries into the alveoli being then expelled to the outside[5].

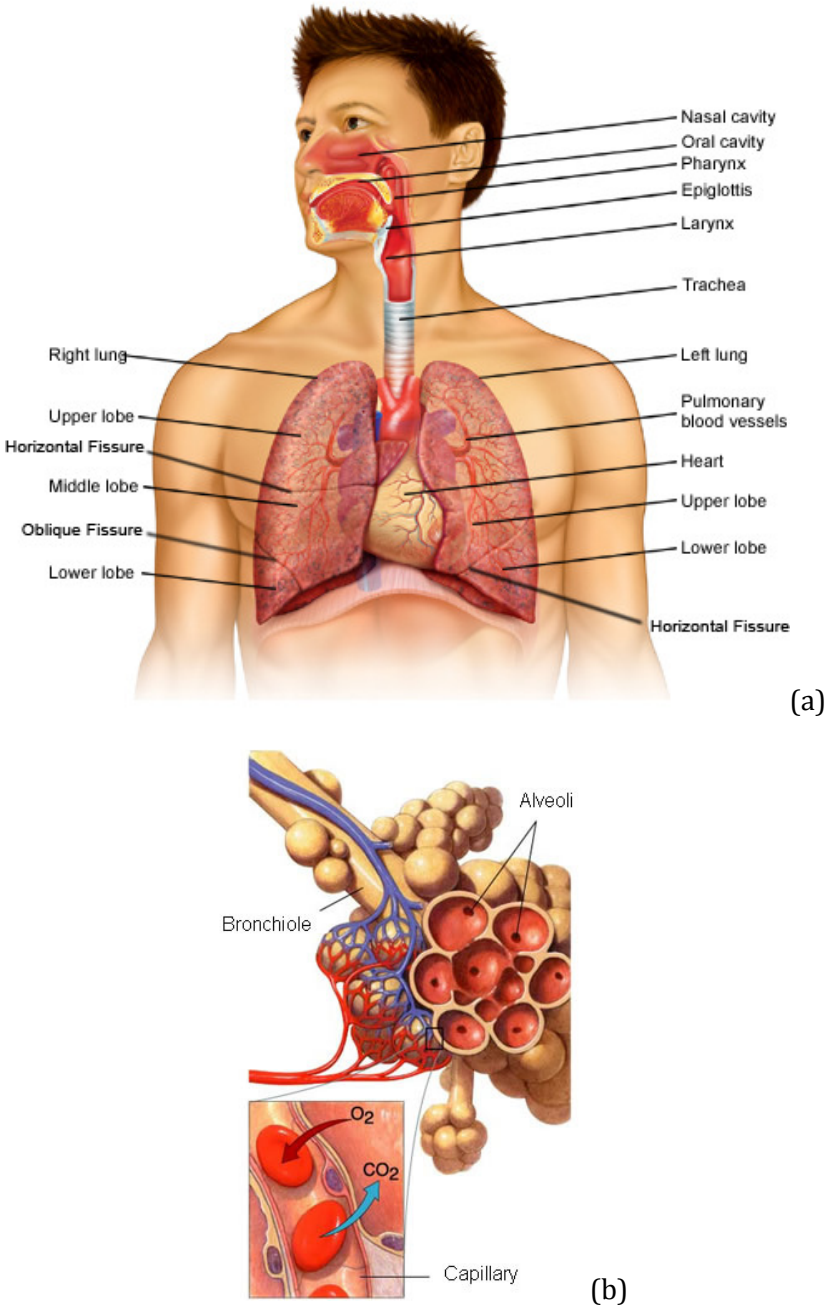

Figure 1(a) Respiratory System [6]. (b) Gas exchange in lungs[7].

A lung is divided into lobes, which are further subdivided into lung segments. The right lung consists of three lobes (superior lobe, middle lobe and inferior lobe) outlined by the horizontal fissure and oblique fissure. The left lung has two lobes (superior lobe and inferior lobe) separated by the oblique fissure (Figure 1 (a))[5].

The localization of the lung segments is difficult, since lungs have not well-defined reference landmarks. There are several anatomical terminologies that are used to describe the distribution of the lung segments. The terminology used in this thesis is based on the E-anatomy website[8]. According to this, the right lung is defined by ten

segments and the left lung by eight segments. The bronchopulmonary segments are characterized as shown in Table 1.

Table 1 Bronchopulmonary segments of right and left lungs

RIGHT LUNG
Bronchopulmonary Segment
Apical (SI)
Posterior (SII)
Anterior (SIII)
Lateral (SIV)
Medial (SV)
Superior (SVI)
Medial Basal (SVI)
Anterior Basal (SVIII)
Lateral Basal (SIX)
Posterior Basal (SX)

LEFT LUNG
Bronchopulmonary Segment
Apicoposterior (SI+II)
Anterior (SIII)
Superior Lingular (SIV)
Inferior Lingular (SV)
Superior (SVI)
Antero-Medial (SVII+SVIII)
Lateral Basal (SIX)
Posterior Basal (SX)

2.2 | Pulmonary Embolism Pathology

A pulmonary embolism, an embolus (also called thrombus or blood clot) can arise anywhere in the body. Usually it moves into the lungs, blocking one of its branches (Figure 2). The severity of the pathology depends on the size of the blood clot and where the blocking is located. An obstruction of the small branch leads to a pulmonary infarction. However, if the main branch is blocked, a massive obstruction can occur or even death[9].

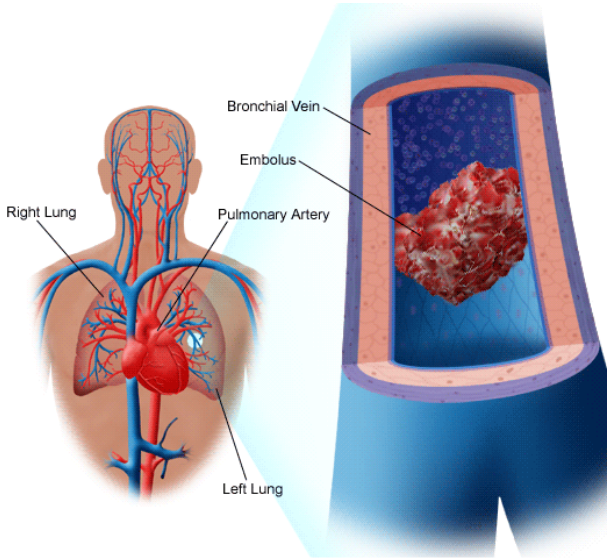

Figure 2 Pulmonary embolism blood clot[10].

There are several risk factors that may be favorable to the creation of a blood clot such as: pregnancy, surgery intervention, heart failure, bone fractures and decreased mobility[1]. As the diagnosis of a pulmonary embolism is very difficult to predict accurately, due to the ambiguous symptoms, several strategies are used to support diagnosis, for example: pulmonary angiography, ventilation and perfusion SPECT studies, multislice CT scanning or magnetic resonance angiography[9].

3 | Imagiologic Modalities

Medical imaging, using several acquisition systems, aims to visualize different aspects of the human body, in order to allow a more rigorous and accurate diagnosis and therapeutic planning. For instance, anatomical structures can be visualized by a CT scanner or a MRI system. Furthermore, nuclear image modalities, such as SPECT or PET provide the detection of the metabolic activity of a specific organ. In this section is given a particular emphasis to CT and SPECT modalities focusing on physical principles, system components, details of the acquisition procedure and the processing and storage of the acquired data.

3.1 | Computed Tomography

The Computed Tomography (CT) analyses the attenuation characteristics of the human body to obtain anatomical information. This scanning system uses X-ray beams that are attenuated when crossing the tissues or organs of the patient. Thus, a CT scanner has an excellent spatial resolution[1] and a large relevance in clinical context.

3.1.1 | Brief Historical Contextualization

The first CT scanner was created by Sir. Godfery Hounsfield in 1972, who, established the beginning of the 1st generation of CT period. The scan pattern of these acquisition CT systems consisted of a simultaneous translation of X-ray tube and a detector (one or maximum two), followed by a short rotation by about one degree. The procedure was repeated until completing the angle range of 180 degrees to 240 degrees. This requires long data acquisition time about 4-5 minutes and a large dose for the patient [11] [12].

In 1974, the 2nd generation of CT scanners was created. The improvements resided in the application of multi-detectors and in the tightening of the fan beam. However, this CT system still needed a translation operation and, despite of the decreasing of the scanning time, it was still very slow: 20s per slice. In 1975, with the

[1]Spatial resolution describes the detail level which can be detected on an image

3rd generation CT scanners, the translation movement was eliminated and, therefore, the entire piece is scanned at once (Figure 3). Using only the rotation movement, it was possible a faster scan, that is, about 1s or less per slice. The incorporation of several hundred or thousand detectors and a thin fan beam (1 to 10mm) guaranteed a significantly improvement on image quality[12].

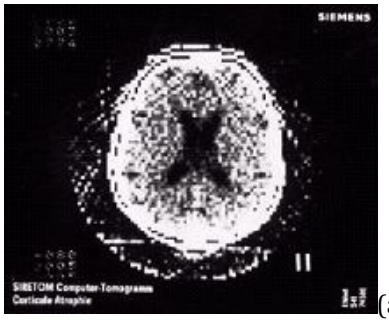

(a)

(b)

Figure 3 Brain CT image: (a) Axial CT image from Siretom CT scanner circa (1975); (b) Axial CT image using a modern scanner[13].

In 1981, the 4th generation CT scanner was introduced in the market. In this acquisition system, only the radiation source had a rotation movement. However, since the detectors should accept rays from different angles, the collimators could not be effective suppressing the scattered radiation and the image quality decreased. The typical acquisition time for large volume body, such as thorax and abdomen, was 30 to 45 minutes[14].

In 1987, the 5th generation CT scanner was developed and it was very similar to the previous. Instead of the mechanical rotation, the radiation source is electronically rotated which improved the position precision of the beam and, consequently, increased the image quality. The acquisition scan could become faster without any mechanical operation[12].

In 1989 the helical technique was developed. In this new improvement, while the radiation tube was rotating around the patient, the patient support was translated through the gantry. Thus, the trajectory of the beam described a spiral. This technique allowed a significantly decrease on the acquisition time - for instance, a complete thoracic exam lasted a 1 minute instead of the previous 10 minutes - and provided a continued volumetric acquisition which improved the three dimensional studies. This technique was enhanced in the following years, by creating multislice helical systems and introducing multiple detector rows in the detection array. This allowed scanning multiple slices in a single rotation. Besides the image quality improvement, this technique provided the selection of slice thickness according to the CT exam[12].

In modern CT systems, the helical and multislice technologies can be incorporated in CT scanners of the 3rd to 5th generations. Thus, large volumes with hundred or even thousand slices can be obtained in few seconds and volumetric information on could be visualized in 3D or 4D The dynamic 4D, also known as cine 3D, gains time relevance and, consequently, motion[11].

3.1.2 | CT scanning system: components and acquisition

A CT scanner consists in an acquisition gantry, essentially composed by an X-ray source tube and a radiation detector; a motorized table and a computer[15](Figure 4). The source tube produces the X-ray beams that pass through the patient, are attenuated and then measured by a detector. The gantry continuously rotates around the patient while the motorized table moves over the gantry, creating a helical acquisition trajectory. From the attenuation measurements, the projective data is computed and the CT image is reconstructed by using a back projection method. All projections are backprojected for each angle into the image region and added all together. In order to avoid the blurring effect caused by backprojection, filtering is used before the projection of data[11] [14].


(a)
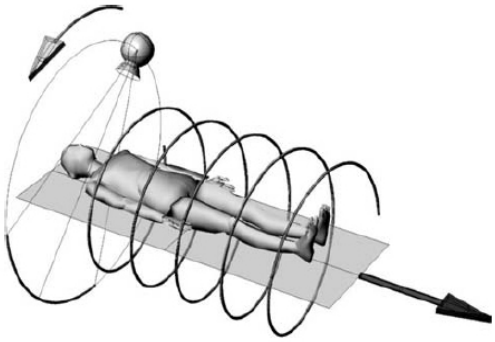
(b)

Figure 4 (a) CT scanning system[16]; (b) a schematic CT image acquisition[11].

CT scans are acquired in axial plan while the patient is in the supine position. 3D anatomical information is obtained by combining the axial CT slices in a stack image. Although CT image is supposed to be in an axial plan, with the application of interpolation methods, the coronal or sagittal plan visualization is possible[14](Figure 5).

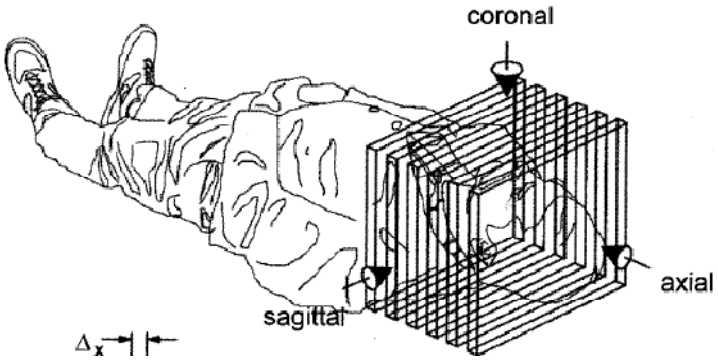

Figure 5 Axial, coronal and sagittal planes of a CT scan [17].

Typically, the images are arranged in a square matrix of 512x512 pixels[2]. The projection of each element in a 2D plane is equal to a pixel, which stores the information concerning the attenuation properties of the tissue. The third dimension represents the slice thickness of the CT scan, varying typically between 1 to 10 mm. The region of interest and the resolution determine the number of slices in a direct proportion[17].

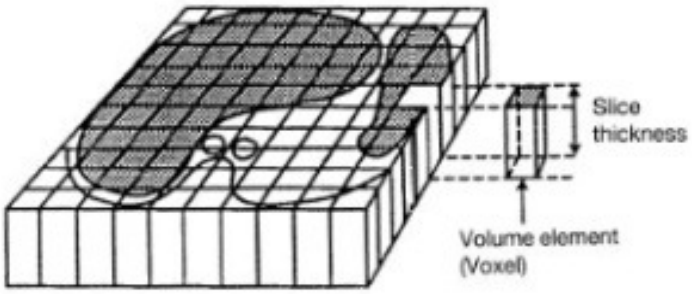

Figure 6 A slice divide into voxels[18].

The attenuation of the beam depends on the tissue properties of the scanned region. For dense structures like bone, the beam is quite attenuated and slight radiation information reaches the detector. The attenuation is measured by a CT number scale expressed in Hounsfield Units (HU) which relates the attenuation coefficients of the material and water. Typically, the CT number scale range is -1000HU for water and 0HU for air. However, depending on the composition and structure this range can be enlarged[14].

$$CT\ number = 1000 \times \frac{\mu_{material} - \mu_{water}}{\mu_{water}} \quad (1)$$

[2] A pixel is a picture element

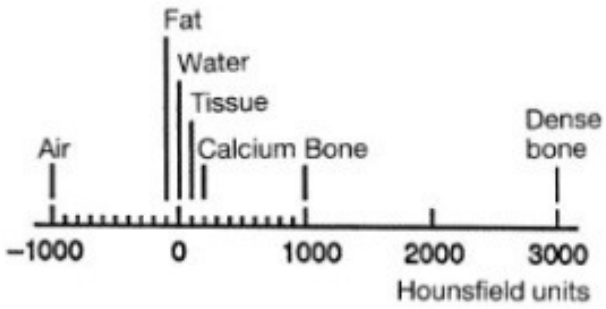

Figure 7 Hounsfield Units scale[18].

The CT exam images can be visualized in order to highlight certain structures. This can be done by defining the window and level settings of the image (Figure 8). The window width and level influence the contrast and brightness of the image. The window width defines the quantity of the display of gray values and the window level is the center defined by a window width range. Typically, to visualize the lungs is used a window/level of 1500HU and -500HU, respectively[14].

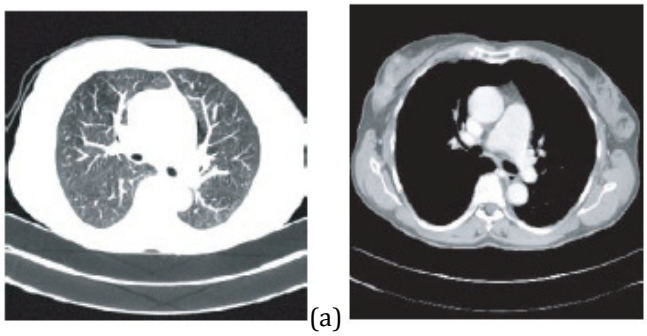
(a) (b)

Figure 8 Thoracic CT image: (a) to highlight the lungs details (width 1500 and level -500); (b) to highlight soft tissues (width 350 and level 50)[14].

3.1.3 | CT scanner: Advantages and Disadvantages

The CT exam has a generic application in the visualization of the bone, soft tissue and blood vessels at the same time in a differentiated and detailed way.

CT scanning is painless, noninvasive and accurate. In a CT examination the X-rays that are used do not have relevant side effects and no radiation remains in the patient after the acquisition. Typically, the effective radiation dose from a CT scanning ranges from 2 to 10mSv (Table 2). Comparing with the worldwide average background dose from cosmic radiation and natural radionuclide in the environment for a human being, which is about 2.4mSv per year, which is much lower than a single CT acquisition exam with the duration of a few seconds[19] [20].

Table 2 Effective radiation dose (E) of several CT exams[14]

EXAM	E (mSv)
Head	1.26 – 1.38
Neck	1.98 – 2.17
Chest	5.17 – 7.01
Abdomen	5.25 – 5.95
Pelvis	7.83 – 9.92

Despite that CT system allows to obtain high resolution images, of soft tissues structures like muscles, organs and tumors, it is required a contrast agent, such as Iodine or Barium, to increase the visibility of those structures[21]. The contrast agents have associated low injurious side effects so the benefits prevail over the risks. Fast acquisition characteristics provide a real time imaging which is very useful in a surgery context. With the cross sectional image acquisition, 3D body images are obtained. Despite this, the acquisition in sagittal or coronal plans requires image reconstruction algorithms, which may cause some quality loss by the computational approximations. Even though CT scanning has some health issues, its performance and the high quality obtained on image results compensate all associated problems[12].

3.2 | Single Photon Emission Computed Tomography

The functional visualization is achieved by the distribution of radionuclides along the body and by the measurement of the radiation. Radioactive tracers are administrated to the patient and travel across the body, gradually concentrating in the target regions. The radiation measure is done by an external scanning system. Positron Emission Tomography (PET) and Single Photon Emission Computed Tomography (SPECT) scanners are currently used in nuclear imaging [22](Figure 9 (a) and (b)).

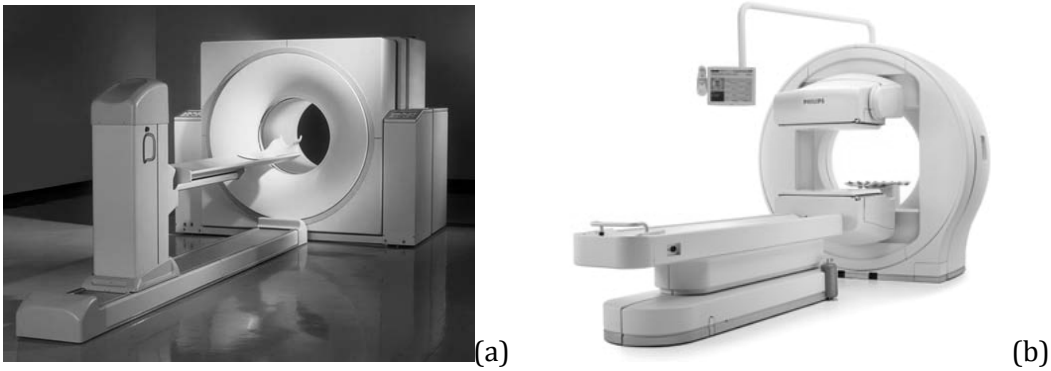

(a) (b)

Figure 9 (a) PET System[22]; (b) SPECT system[14].

Concerning PET, the administrated radioactive tracer interacts with a body tissue, decays and emits positrons. Each positron annihilates with an electron producing two photons that will be emitted in opposite directions. These photons will be detected and then the image is created. In SPECT, the interaction of the radionuclide with the body tissue only emits a single photon. Apart from operating technology differences, where PET scanner is based on cyclotron (charged particle accelerator) and SPECT on a Gamma Camera, the radioactive substances applied in SPECT scanning have longer half lives than the used in PET. Therefore, it is possible a better handling. PET systems are more expensive but provide more detailed images than SPECT. Further on, it will be given more emphasis to SPECT system, since this work is focused on images acquired in this modality and CT scanner [22] [23] [11].

3.2.1 | Brief Historical Contextualization

The origins of SPECT scanning are related to the use of radioactive isotopes for medical purposes in the 1920's. In the 1940's, using a single detector positioned at several spots around the head, it was obtained radioactive source distributions within the brain. In 1958, Hal Anger developed the Anger Camera, which is the base design of the modern acquisition systems (Figure 10). At this time, this device produced 2D planar images. The Gamma Camera detects and counts the photons emitted by a radionuclide. With the information of the position and energy, an image of the activity distribution was created[14].

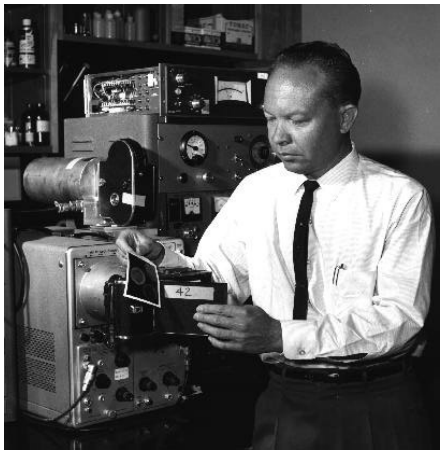

Figure 10 Anger with a Gamma Camera[24].

In 1963, Kuhl and Edwards developed an adaptation of Gamma Camera that allowed producing tomographic images. By the rotation around the patient, multiple images were formed and tomographic characteristics were obtained[22].

In 1968, a device called MARK IV was the first Emission Computed Tomography (ETC) system developed. This scanner contained a Gamma Camera with multiple sodium iodide detectors arranged in a rectangular shape[22].

In 1972 was developed the first commercial SPECT system called Tomomatic 32, in which the Gamma Camera had 32 detectors. Despite the quality of the resulting images, that was not enough and it was discarded its clinical application. In 1976 John Keyes and Ronald Jaszczak developed an improved rotating Gamma Camera. In 1977, Everett, Fleming, Todd e Nightengale, using better correction methods for Compton Effect[3], were able to minimize it and thus decrease the image blur obtained so far. The improvements of the Gamma Camera and the correction of Compton Effect made possible to achieve significant advances in the performance of SPECT scanning system[14].

In 1999, GE Medical Systems developed the first hybrid SPECT/CT system for clinical applications. This scanner provided functional and anatomical images in the same scanning session, which facilitated the alignment of SPECT and CT images and then anatomical recognition[25]. Recently, SPECT scanners have been miniaturized to Micro-SPECT systems to allow imaging studies on small animals and the visualization of biological processes and pharmacological activity of drugs in vivo[26] (Figure 11).

Figure 11 Micro-SPECT system[27].

3.2.2 | SPECT scanning system: components and acquisition

A SPECT system measures the metabolic activity of a tissue or organ. In this modality, a radionuclide tracer is administrated to the patient and, when it interacts with a target body region, decays, emitting radiation gamma that is detected by a Gamma camera. SPECT scanning produces cross-sectional images which are acquired by rotating the camera with circular or elliptical movements around the patient and getting multiple projections from various angles (Figure 12). As in CT, SPECT projective data is

[3] Compton camera: A Compton camera uses two gamma detectors operating in coincidence in order to avoid the inherent scattering (Compton) effect when the single photon interacts with the body tissue or organ target.

reconstructed to form the final image. By combining 2D slice images, 3D image is obtained. Typically, Gamma Camera rotates 3-6 degrees around the patient, each projection lasts 15 to 20 seconds to be taken and an acquisition session about 30 minutes. SPECT acquired data is stored in an image matrix of 64x64 or 128x128 with a variable number of slices. In general, the slice thickness is 5mm. Pixel value represents the number of detect photon count emitted by the target tissue or organ. SPECT images cannot be acquired in 512x512 pixel format like CT images since, in order to achieve that resolution, a large amount of tracer has to be administrated and that would be injurious to the patient [14] [22].

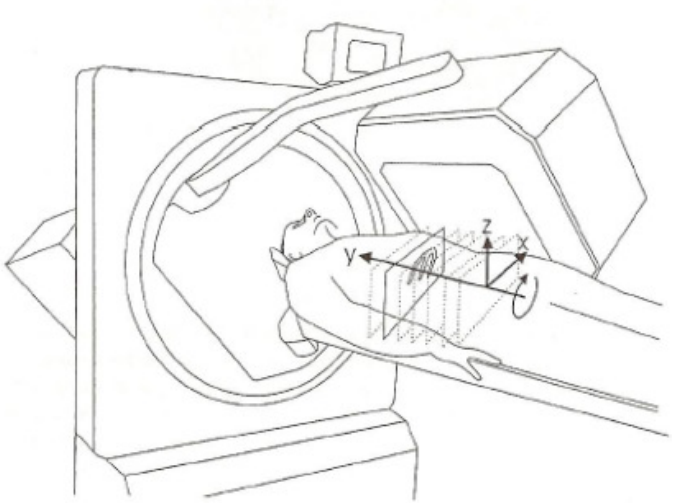

Figure 12 A schematic SPECT acquisition[14].

SPECT scanners can have different configurations according to the imaging exam goal. The number of head cameras used is crucial to the sensitivity of the acquisition system. Using simultaneously a large number of heads allows an increasing detection of photon moving on abnormal trajectories that otherwise could not be detected and, consequently, would be important information losses on the resulting image. Usually, for brain studies, it is used a triple head SPECT camera and two head cameras to myocardium or lung exams (Figure 13). Most of SPECT scans have 360º orbit acquisitions. The acquisition can be performed using a step-and-shoot process or a continuous process. In the first mode, the camera head starts rotating and stops at defined positions, waiting at each position while data is acquired and then moving on to the next position. Concerning continuous mode, the camera head rotates continuously around the patient. The step-and shoot provides better resolution and continuous acquisition is more efficient[22].

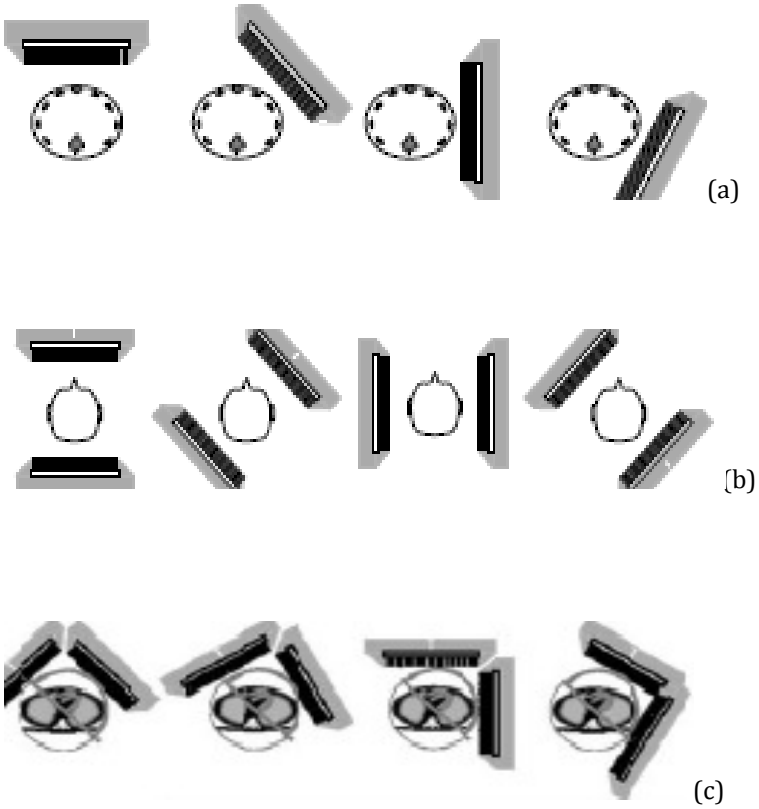

Figure 13 Camera locations: (a) bone SPECT acquisition, (b) brain SPECT acquisition and (c) cardiac SPECT acquisition[22].

SPECT acquired images characterize the activity distribution of the radionuclide in a target tissue or organ. The radionuclide can be administrated to the patient by intravenous injection, orally or aerosol inhalation. The radionuclide is a molecule which contains an unstable isotope (tracer) that emits gamma rays. The most used tracer is the 99mTc. It has a relative short half-life, which allows an acquisition scanning and keeps radiation exposure to low levels. This radioisotope has ideal emission energy (140keV) which is high enough to leave the body and be detected by Gamma Camera. 99mTc tracer has a low cost to produce. The application of a radionuclide depends on the study exam (Table 3). The half-life must be adjusted to the duration of the tracer administration procedure and acquisition process. The amount energy required for the photons to leave the target region has to be enough to be detected by Gamma camera [28] [29] [30] [31].

Table 3 Several SPECT examinations and respective radionuclide [14]

STUDIES	RADIOISOTOPE	ENERGY EMISSION (keV)	HALF-LIFE	EFFECTIVE RADIATION DOSE (mSv)
Lung Perfusion	99m Tc MAA[4]	140	6 hours	1.6
Lung Ventilation	99mTc-DTPA[5]	140	6 hours	1.8
Thyroid diseases	I-123	159	13 hours	4.8
Prostate cancer	In-111	171	3 days	2.6
Heart	Th-201	70	3 days	17
Tumor	Ga-67	93	3 days	12.2

3.2.3 | Ventilation/Perfusion studies and Pulmonary Embolism

A lung study requires two successive acquisitions resulting on two sets of data information. When doing the ventilation scanning, the patient inhales an aerosol of 99mTc-DTPA for a few minutes before the acquisition process. During this procedure, the radiotracer distribution is detected and an image is created. Ventilation lasts for about 5 minutes and its end coincides with the beginning of the ventilation data acquisition. A 99mTc-MAA tracer is injected to the patient and a lung distribution tracer image is acquired. Usually, the total acquisition scanning is performed during 30-60 minutes. When the perfusion is applied, the inhaled tracer is still retained in lungs although the injected tracer amount is bigger. To eliminate the component of the ventilation data on the resulting image, a subtractive operation is performed after the total acquisition process[22].

This procedure is commonly used to detected pulmonary embolism. In the case of a non pathologic patient, ventilation and perfusion SPECT exams would be similar. The injected tracer could travel through all pulmonary regions without any constraints. Concerning an embolism patient, a mismatch between ventilation and perfusion scans is detected. In PE, a clot is formed anywhere in the body and travels to lungs over the bronchopulmonary tree, blocking capilars or major arteries in the lung tree, affecting blood circulation. The blocked area will be identified by comparing the ventilation and the perfusion SPECT exams and detecting the deficiency of non tracer deposition in the perfusion scanning [14].

[4] Technetium-99m macroaggregated albumin
[5] Technetium-99m diethylenetriaminepentaacetic acid

3.2.4 | SPECT scanner: Advantages and Disadvantages

Once SPECT scanning uses radioactive tracers, it has inherent health risks associated, including overdose and contamination. When a radiotracer is administrated, it will not only accumulate in a specific target, but wherever it travels through. Another disadvantage of this technique is that the tracer still remains in the patient for a while after the acquisition exam. The remaining time of radiation in the body will vary according to the patient metabolism and the proprieties of the tracer[14].

Imaging limitations of SPECT systems are related to scattering, attenuation effects and the radiation dose amount. Scattering effect can cause measurement errors on emission photons positions. Once a certain amount of emitted photons interacts with tissue or organs and is attenuated, a substantially data information will be lost. Attenuation effects affect the image quality. Image contrast[6] and resolution are influenced by the tracer dose used during the acquisition and the radiation exposure of the target region. An incorrect alignment of the Gamma camera position and detector scratches can introduce image artifacts, such as dead pixels or unread lines that influence the quality of the resulting image[22].

Despite that SPECT scanning produces low quality images; its cost is more affordable than other nuclear medicine techniques, such as PET. The radioisotopes applied to SPECT exams have a long half-time that allows its easier manipulation[14].

[6] Image contrast is related to the ability to detect slight changes in luminance of regions without defined contours

4 | Image Processing: Theoretical Background

Medical imaging allows, using a non-invasive technique, to obtain information about the human body. The possibility given by the 3D images of the region of interest has high relevance concerning applications such as surgery planning for extraction of a region or structure or even in real time acquisition during surgery. In order to enhance proprieties or details of the image, processing methods are applied[14] [32]. This chapter covers some segmentation and registration methods and it presents an overview on the literary work that has already been performed.

4.1 | Segmentation

Segmentation is the process of extracting important information from an image [11]. In this section, it is introduced the principles of segmentation and its applications on medical imaging. On the second part of this section, the state of the art is presented, focusing CT and SPECT image segmentation.

Segmentation is a technique that allows identifying regions in an image which have specific properties such as color, intensity or texture. Segmentation is widely used on boundaries detection, region of interest extraction and image measurements. In pulmonary studies, segmentation process is most applied to the extraction of pulmonary regions and to the identification of the pulmonary boundaries and organs[33].

Several methods can be used depending on the goal of the analysis. Segmentation can be done manually or automatically, on an entire image or on sub region of the image. There are three segmentation categories: they can be based on threshold, based on pattern recognition and based on deformable models [34]. The most applied is the threshold-based method, due to its simplicity, fast performance and satisfactory results produced. Although, it shows low efficacy on processing images affected by noise or images with low contrast. When using this method, a threshold condition is defined and the image is divided into groups of pixels, according to their values and relation with the threshold. The condition can be select manually or based on a value from the image histogram. This method can be applied globally, based on histogram or local properties; locally, allowing to separate relevant regions when the

image background is not homogenous; or even with dynamic threshold in which for each group of pixels is defined a local threshold [33]. Region growing segmentation is a threshold-based algorithm. This algorithm typically requires a set of seed points for initialization and searches for adjacent pixels. When its intensity value matches with the threshold condition, the pixels are jointed to expand and create a region [35]. Another used algorithm is the edge-based segmentation in which structures or boundaries of the region of interest are defined by the local pixel intensity gradient. The main disadvantage of this method is that in most cases, the edge identification does not enclose totally the region of interest, creating a discontinuity. Therefore, it may be required a manual post-processing step of edge linking[33].

The segmentation based on pattern recognition identifies structures or regions using pattern information from intensity, position and shape of an image. This method can be supervised or unsupervised. Supervised artificial neural networks, support vector machine and active appearance models are examples of supervised segmentation[34]. These methods are initialized with a learning step in which is used a classifier with a training set, as a learning algorithm, and a target function, in order to extract pattern information to define criteria parameters. Later on, when making the recognition step, the input image is compared to the trained data and it is performed the searching of the best match to the defined pattern information criteria. On the unsupervised algorithms is not applied the learning step, therefore any pattern data information is previous known. The segmentation process involves a clustering approach that gradually creates similar groups of pixels. Unsupervised neural networks and Fuzzy C-Means algorithms are pattern-based segmentation methods. Despite showing better results than the threshold-based, the pattern-based methods are also sensitive to noise effect and it is much influenced by the initial parameters[33].

The segmentation based on deformable models consists on a boundary delineation of the region of interest represented by a curve or surface defined from an image. The deformable models are influenced by internal and external forces. The internal forces are characterized by the curve or surface and maintained the smoothness of the model during the segmentation process[34]. The external forces allow travelling of the deformation model until it reaches the boundaries of the region or structure of interest. Related to the curve, there is an energy function. The segmentation is performed by searching the boundaries in order to minimize that energy. The deformable models-based methods can be parametric or geometric models[34]. The parametric methods are defined by parametric curves or surfaces. A previous

knowledge of the target shape is needed before the segmentation process, since the parametric algorithms are not sensitive to the topology of the region of interest. The parametric behaviour allows a compact representation which is very useful for real-time applications. Snakes are an example of this type of deformable model. The geometrical model is based on a curve evolution that is related to the geometric characteristics of the region of interest. This model adjusts to the topology of the target and it can easily adapt to its shape. The level set algorithm is a geometrical deformable model. This method is powerful for complex segmentation [33].

4.1.1 | State of the Art

Over the years several works have been done in image segmentation accomplishing different results according to the purposes. The state of the art is focused on segmentation of CT and SPECT images.

4.1.1.1 | Segmentation in CT Images

Sun et al. [36] purposed a 3D segmentation and visualization method by using single detector CT images for detection and diagnosis of lung cancer. The segmentation was based on 3D region growing. The method started with a seed selection by applying either manual or automatic approaches, in which the user can select the seed points by using an interface, or using a fuzzy logic algorithm (fuzzy C-means) to automatically locate these points. In this method, a growing criteria selection was done based on region homogeneity, region aggregation and gradient magnitudes of the voxels. An automatic threshold was purposed based on the volumetric histogram and intensity and gradient curves. An analysis of the volumetric histogram allows to detect the intensity value of the lung voxel and thus an optimal threshold was determined. In order to generate segmentation mask it was used an auxiliary cubic volume. Since the results obtained by the purposed method could show an incomplete extraction of the lung volume, morphological methods of dilation and erosion were applied. The lung extraction results were compared with the corresponding gold standard and it was possible to conclude that the method was more effective and robust than the gold standard.

Lei et al. [37] presented a fast lung segmentation method for computer-aided diagnostic (CAD) system on thoracic CT image. The purposed method initialized with a pre-processing step that excluded the pixels which were out of region of interesting, by setting them to zero value. For each CT slice, it was determined an optimal threshold,

using an interactive process which combined the maximum gray-level number and the minimum gray-level number of the image. In order to avoid the error caused by outside ROI pixel values, the pixel number of the image was also included. Therefore, a binary image was created. Morphologic operations were applied to the resulting images and non pulmonary parenchyma was eliminated. If the left and right lungs were not successfully segmented by using the optimal threshold, it was applied a fast location of the joint region or a self-fit re-segmentation based on watershed algorithm[7]. In order to eliminate non-smoothness edge and small cavities inside the lungs, it was applied a segmentation refinement and, after an erosion operation, the segmented lung was obtained. The purposed method was tested on CT slices of 30 patients. The results obtained showed that, in 90% of the images, the left and right lungs were correctly segmented after the threshold, without needing any re-segmentation. The results were compared to a manual segmentation done by an expert and showed that the results were quite similar. The method allowed applying overall lung parenchyma segmentation and retaining the detail.

Zhou et al. [38] purposed a fully automated segmentation and classification method to identify lung anatomical structures using high resolution chest CT images. The method was applied along five main steps. The first step was to segment and divide the regions over the whole lung of CT images through a histogram analysis and a gray-level thresholding method, by using the density distribution to identify the region of interest. An optimal threshold value was automatically determined for each CT image slice. Then, it was applied the extraction of the trachea and bronchi and the recognition of the bronchial tree. The airway region was gradually expanded by increasing the threshold value until the segmented region achieved the lung. The extraction of the total airway region was based on a branch-by-branch process and, for each one, it was determined an optimal threshold value. The regions were validated by comparison to the anatomical references of structures of airway trees. Then, the lung region was extracted and the left and right lungs were separated by applying region shrinking algorithms. The following step was to extract pulmonary vessels by applying a similar algorithm to the extraction of the bronchus region. After that, the lobar bronchus and vessels were recognized and used to divide the lung regions into lung lobes, by detecting the edges of estimated fissure locations. This method was tested in 44 patients and the obtained results showed that the method successfully classified and recognized lung structures from 41 patients.

[7] Algorithm based on growing regions

Pu et al. [39] used an adaptive border matching to perform lung segmentation in lung nodule computer-aided detection from chest CT images. The purposed method was based on a smoothing process of contours in continuous space. The method started with a removing step of non relevant acquisition information, such as isolated pockets of air, by using a Gaussian smoothing. Then, a gray-level threshold was performed with a -500HU cut-off. After the threshold step, 2D flooding operation was applied in each slice in order to remove non-lung regions. Several directed closed contours were generated by tracing the border of the lung region in a sequence of pixels. Then, in order to locate the over segmented regions and overcome their limitations, it was applied an adaptive marching step length based on Euclidean distance which introduced an adaptive behaviour to the threshold value. The purposed method was tested in 20 datasets of CT images and showed to be robust, efficient, with low computational cost.

Kakar et al. [40] used a texture-based segmentation and recognition method to detect lesions in 3D CT images of lung cancer patients. A pre-processing step was performed by using a median filter to remove the acquisition noise and a contrast enhancement technique was applied, by mapping intensity values to new values, in which 1% data was saturated at low and high intensities. The segmentation step started with the application of a Gabor filter which allowed to extract textures features in the image. Since the boundaries of lesion were not clearly defined, the features were combined and a Fuzzy C-Means clustering was performed. Thus, the target volume was segmented. In this method an optimal number of 15 clusters were used, which was determined empirically. The recognition step involved features extraction combined with a learning phase in which the algorithm used for the texture content image data was trained, and a recognition phase in which the textural features were compared to the training images with a classification algorithm using Support Vector Machine. In order to evaluate the performance of the method, accuracy and sensitivity were measured. This method was tested in 42 images from different lung cancer patients. The obtained results showed an accuracy of 94.06% for the left lung, 94.32% for the right lung and 89.04% for lesion. The classifier algorithm presented an average sensitivity of 89.48%.

4.1.1.2 | Segmentation in SPECT Images

He et al. [41] performed an Image Analysis System to identify the left and right pulmonary lobes by using Perfusion-Ventilation SPECT scans. In order to recognize the pulmonary region from the SPECT scans and separate it from the background, minimum

cross-entropy threshold segmentation was applied. The optimal threshold was determined from the cross-entropy distance based on probability distributions. A watershed algorithm was used to separate the left and right lungs. This algorithm started by dividing the SPECT image into several regions and subtracting the detected central region. The next step consisted on applying an edge contour extraction to the lung lobes, using a contour tracing, travelling through each image from top-left to bottom-right to find the edge points. Then, it was performed the pulmonary lobe partition step, in which each lobe was divided into 9 regions. The height and width of the pulmonary lobe were measured and divided based on average. In order to compare the function of different regions in Perfusion and Ventilation SPECT images, radiation counts were performed. This method has powerful applications in pulmonary embolism and lung cancer diagnosis.

In literature, segmentation is widely applied has a pre-processing step for SPECT/CT registration of pulmonary scans, using a simple threshold. Takenaka et al. [42] on a study to predict lung volume reduction of surgery candidates used a pre-processing segmentation step in which a threshold of 15% of the maximum radioactivity was used to defined the lungs contour of the SPECT exams. This work consisted in a performance comparison between perfusion SPECT scan, registered SPECT/CT images, CT quantitatively and qualitatively CT images. Suga et al. [43] purposed a study of the functional mechanism of lung mosaic computed tomography attenuation in pulmonary vascular disease and obstructive airway disease. This study was performed by using deep-inspiratory breath hold perfusion SPECT/CT fusion images and non-breath-hold SPECT scans. To obtain the SPECT lung contours were applied a threshold of 10% of the maximum radioactivity of the lungs.

Palmer et al. [44] purposed a method for assisting the diagnosis of pulmonary embolism by using ventilation and perfusion SPECT exams. The method initialized with the elimination of hotspots on the ventilation SPECT by using a clearance correction. The hotspots could be created by extra-pulmonary activity of trachea or stomach deposition of contrast agent. Through the histogram, it was calculated a threshold of 25% maximum, in order to find pulmonary region contour and identify the left and right lungs. Since the perfusion was acquired after ventilation, during the perfusion scanning, the aerosol activity was still detected. Therefore, it was done a subtraction of ventilation on perfusion scans. Then, rate normalization counting was applied to ventilation and perfusion SPECT exams and the ventilation/perfusion quotient was calculated. Subsequently, ventilation, perfusion and quotient images were analyzed to detect

mismatches between them, which might indicate any pathologic region. This method was tested in 15 patients and showed a fast performance and to be supportive to diagnosis of obstructive pulmonary diseases.

4.2 | Registration

Registration allows the overlaying of two or more images. In this section, it is reported an overview of registration processing and a brief approach to what already exists in the literature, focusing on lung SPECT/CT images registration.

Image registration is a powerful aim to medical imaging. This process consists on the alignment of two images in order to establish a correspondence between them and, therefore, visualize and analyze them in the same spatial system. During the registration process, the moving image is deformed to be adjusted and fit to a reference image. The registration can be applied to a mono-modality context, i.e., using images from the same imagiologic modality. For instance, this is very useful to analyze the tumour evolution of a patient, in which images are acquired in different times. Using registration alignment they can be then compared. In a multi-modality context, it is possible to combine different data information, for example, functional and anatomical information, and, then, improve the medical diagnosis. Registration process is also applied for getting correspondence between acquired images and a reference medical atlas [11] [45].

The registration algorithms can be categorized by the registration basis, transformation algorithm or the domain of transformation. The registration basis is related to the relevant points or regions of interest which will act as reference elements for the images alignment. Registration can be performed by using landmarks, which are well known points that can be marked on the patient during the exam acquisition or can be identified in the acquired image. By applying similarity measures between the images, the alignment can be based on segmentation of binary regions or voxel based. The transformation algorithm used in registration represents the method as the moving image is aligned to the reference image, according to the degrees of freedom, and the deformable characteristics. The transformation can be rigid body, where is allowed six degrees of freedom (rotations and translations in the x, y and z axes), while in the affine registration it is possible to have twelve degrees of freedom (rotations, translations, size scaling and shearing in the x, y and z axes). A non-rigid transformation has an elastic nature which allows a greater deformation. The greater the transformation complexity, higher will be the computational cost and the processing time [45]. The registration can

be performed globally when the transformation is applied to the entire image or locally when for different regions in the image are applied specific transformations.

In conclusion, to describe a registration algorithm, required three main elements are required: transformation model, similarity metric and optimization process [33]. The transformation model, as described above, is related to the alignment behaviour of the moving image to be adjusted to the reference image. The similarity metrics quantify the differences between the reference image and the registered moving image. Correlation and mutual information are examples of metrics. Correlation gives intensity relationship between the two images and mutual information defines a probabilistic relation with the intensity of the images. The optimization process varies the transformation parameters in order to maximize the alignment between the images. Iterative closest point is a very used optimization algorithm, in which interactively minimizes the distance between points of the two images [46].

4.2.1 |State of the Art

Several registration methods have been reported in literature. In this state of the art is presented some works about mono and multimodality registration in an intra and inter patient context.

Woo et al. [47] purposed a 3D registration method to be applied on myocardial perfusion SPECT and coronary CT angiography images to help the diagnosis of coronary artery disease. The registration was performed by using 3D segmented SPECT images, where regions of myocardium and blood pools were extracted and used as an anatomical mask. A Gaussian filter was used to homogenize the intensity levels, to lower the CT image resolution and to remove image noise. A 3D registration transformation was applied using 3 translation parameters and 3 rotation parameters. In this work it was purposed energy functional based on the segmented SPECT volume which related constants parameters of average region intensities, a Gaussian kernel and the rigid transformation parameters. To minimize the purposed energy functional, the optimal values of the constants parameters and the standard deviation were determined by using a gradient descent algorithm based on Euler-Lagrange equations. The purposed registration method was compared to a Normalized Mutual Information method and a manual alignment done by 2 observers. The obtained results showed that the purposed method has a good performance and could be successfully applied on clinical practice.

Song et al. [48] performed an optimization method for non-rigid image registration using a multi-metrics routine. Often, during the optimization step, an error

on the assessment of local minima leads to wrong registration results. The purposed method allowed to avoid incorrect registration by using a multi-metrics model that was automatic adjustable during the registration process by switching between metrics, in order to obtain the best optimization. In this work, it was done mono-modality (MRI-MRI) and multi-modality (CT-MRI) registration by using brain images. A non rigid algorithm using B-spline transformation was applied. For MRI-MRI registration, it was used a 10x10 control grid for 2D images with 256x256 matrix size. For CT-MRI registration, it was used three types of control mesh: 6x6, 10x10 and 14x14 for 2D images with size 250x250. Metrics applied for mono-modality registration were Mutual Information (MI), Mean Squares (MS) and the multi-metric model MI&MS. For multi-modality were applied MI, Normal Vector Information (NVI) and the MI&NVI multi-metric. As an optimizer, it was used the L-BFGS-B method, which had the advantage of speed performances on minima research. Registration processes were evaluated according to run time and to image similarity measurements. On both methods (MRI-MRI and CT-MRI), registration using MI had the faster performance, but the obtained results did not show a good alignment. This occurred due to the failure of the metric on finding the local minima. On MRI-MRI registration, using MS allowed to achieve good registration results, despite the fact that the processing time was high. On CT-MRI using NVI beyond the computational costs, the obtained results were worse than the MI results for the same registration method. For both methods, the respectively multi-metrics model had low processing time and good registration results. The obtained results showed that the purposed multi-metrics registration method was robust and fast.

Pan et al. [49] developed a method to estimate regional lung expansion by using 3D CT images of sheep lungs. This study was performed in 3D CT images of two sheep with 512x512 matrix size. Images were acquired in a multi-detector row CT in prone and supine positions at several different airway pressures (0 to 32 cm H2O). The algorithm was initialized with a pre-processing step, where it was performed lung segmentation to extract lung boundary and airway tree segmentation to detect bronchi landmark points. Then, the image data was resampled to 256x256. The registration step was applied using lung surfaces and the airway landmarks as control points, performing on four resolution levels varying from 0.0625 to 0.5 of full size. Registration was validated by the landmark error, which was related to the registration error at the registration landmarks, and the volume overlap error. The last step of the method was to compare and evaluate the lung expansion obtained by the several registration procedures. Lung expansion was detected by visual inspection of the deformation file

created during the image registration. This method showed that, at a lower pressure, the regional lung expansion was higher than at higher pressure.

A study of rigid registration using intra patient 3D images of CT, PET and SPECT exams for identification of changes in tumour localization was presented by Hahn et al [50]. Their method included an automatic extraction of 3D salient region features; an estimation of corresponding regions by using an optimization of a joint correspondence set based on a local intensity similarity; and outliers elimination by using an accurate refinement at sub-pixel level. A hybrid scanner was used to image acquisition. This study used 11 PET-CT 3D images acquired at different times, 3 CT 3D images acquired at different times of the treatment and 10 SPECT-CT 3D images. The method was evaluated by an expert by measuring the distance between a set of selected corresponding points, such as anatomical and functional structures or lesion sites. The obtained results showed that the method is robust and could be applied as additional element in a non-rigid registration procedure.

Yin et al. [51] evaluated different registration algorithms by using low resolution CT exams acquired from a SPECT-CT hybrid scanner, planning CT exams and a SPECT exam, for radiation therapy treatment planning. A 3D registration method was applied between low resolution CT exams and planning CT exams by using a rigid transformation in order to maximize the mutual information of the two exams. They also applied 3D CT-CT affine registration based on manually selection of control points in the lung volume and on the skin contour. Another method of CT-CT alignment was presented by using rigid registration followed by B-spline transformation. A control point grid was applied and manipulated to maximize the mutual information measure by using an optimizer based on a gradient descent. After the CT-CT registration procedures, the SPECT images were warped and registered, as reference image, to the planning CT exam. These registration methods were tested in planning CT images with a 512x512 matrix size that were down-sample to 256x256 (a pixel size of 1.875x1.875x5 mm^3); low resolution CT with 256x256x40 matrix size(a pixel size of 2.2x2.2x 10 mm^3); and SPECT images with a 128x128x128 matrix size (4.4x4.4x4.4 mm^3). In order to evaluate the registration similarity was applied the root mean square of intensity differences, the median absolute deviation of intensity differences and the maximum intensity differences. This study showed that the B-spline registration provided accurate results to radiation therapy treatment planning and that the point based registration was better for lung deformation detections.

Papp et al. [52] purposed an extension of the normalized mutual information method applied to SPECT/CT registration of lung images. A hybrid SPECT/CT scanner was used to acquire at the same time, the low dose CT, ventilation and perfusion SPECT scans of twenty three patients. All images were resampled to 1x1x1mm voxel size. Between SPECT images, it was applied a histogram matching in order to increase the intensity similarity. Then, SPECT and CT images were scaled between 0 and 255 to decrease further entropy calculation time. The registration step started with a misalignment simulation of the CT images by using a known rigid transformation. Then, misalignment CT image was registered to the ventilation and perfusion SPECT images by applying the purposed extended normalized mutual information-based method. To evaluate the performance of the purposed extended method, a registration using dual-normalized mutual information-based method was applied. The obtained results were compared and the registration error was determined. This comparison showed that the purposed normalized mutual information method obtained lower registration errors and could be applied to SPECT/CT registration clinical routines.

5 | Methodologies

To obtain anatomical information on the patients suspected of pulmonary embolism, it was performed the registration of 3D SPECT images with the 3D CT image of a reference lung. The CT exam has anatomical information about the thoracic region and the SPECT exam has functional information about the pulmonary airflow (ventilation) and blood circulation (perfusion). For this study, the following types of images were used:

- CT scan of a lung reference
- Binary images of the pulmonary region from the CT scan (used on the registration process)
- Binary images of the bronchopulmonary segments from the CT scan (applied to identify lung segments)
- Ventilation and perfusion SPECT scans of four patients (used in the identification of lung segments)
- Quotient V / P SPECT, obtained from the ventilation and perfusion SPECT scans, which allow to detect mismatches between the ventilation and perfusion scans (used in the identification of lung segments)
- Binary images of ventilation and perfusion SPECT scans of the pulmonary region (used on the registration process)

The methodology starts with a segmentation procedure to extract relevant information from both CT and SPECT (ventilation and perfusion) scans, i.e., to extract the pulmonary region, and producing a 3D binary image. For each SPECT exam, the binary image, which corresponds to the pulmonary region, was computed using the ventilation and perfusion SPECT exams. The registration process used rigid (rigid body, global rescale, specific rescale and affine) [53] and non-rigid transformations (diffeomorphic demons) [54]. During the registration process, SPECT image was the moving image and CT image the reference image. After the alignment of the binary SPECT and CT images, a transformation matrix was obtained for each registration algorithm. After analyzing the performance of the several registration algorithms, the affine transformation was chosen to be applied in the identification of suspected

pathologic bronchopulmonary segments. By applying this transformation matrix on ventilation, perfusion and quotient SPECT images, these images became aligned to the SPECT binary image obtained after the registration process. Therefore all SPECT images were aligned. This means that these images were also aligned with the CT image (reference image on registration process). Thus, as the CT binary image was aligned with the CT image of the bronchopulmonary segments, all SPECT images were aligned with the two CT images. This would allow comparison between the SPECT images and CT image of the bronchopulmonary segments to identify the suspected pathological segments. By comparison between the aligned SPECT images and the bronchopulmonary CT segments, it is possible to: (1) detect the characteristic mismatch of pulmonary embolism of ventilation and perfusion SPECT images; (2) compare the mismatch with the quotient SPECT image and (3) identify in the CT image the bronchopulmonary segment with suspicion of pathology.

In this section are reported details of images acquisition, segmentation and registration processes, and the identification of the pulmonary regions suspected of pulmonary embolism.

5.1 | Image Data and Pre-Processing Procedures

5.1.1 |CT Image of Pulmonary Region

From E-anatomy website [8], a CT scan of a lung was obtained, which was considered the reference exam for the present study. The exam has the dimensions of 550x550 pixels with 87 slices. Since SPECT scans were acquired with a size of 64x64 pixels and a total of 64 slices, CT scan was resampled to 64x64x64 (Figure 14(a)).

A segmentation pre-processing step was used to identify the pulmonary region. In order to attenuate the noise that could induce an incorrect detection of the lung contours during the segmentation, a Gaussian filter was applied. Then, a threshold with a cutoff -500HU was used. This cutoff value was obtained experimentally analyzing histogram charts of several CT exams and having in consideration the range of Hounsfield Units for the lungs: -950HU to -550HU [55]. The CT scan from E-Anatomy website [8] was in grayscale (0-255 intensity values), which corresponds in Hounsfield Units (HU) to a range of -1000 to 2000HU. By extrapolation, the cutoff value in grayscale was determined. To eliminate any existing interior holes in the pulmonary region and exterior holes due to trachea morphological operations were applied (Figure 14 (b)). The segmentation method was applied to each CT image slice. The 3D CT binary image

consists on associating all slices into a stack. After obtaining the binary image of the pulmonary region, right and left lungs were separated so that registration could be performed individually for each lung, since the variability of the distance between them depends on the patient (Figure 14 (c) and (d)).

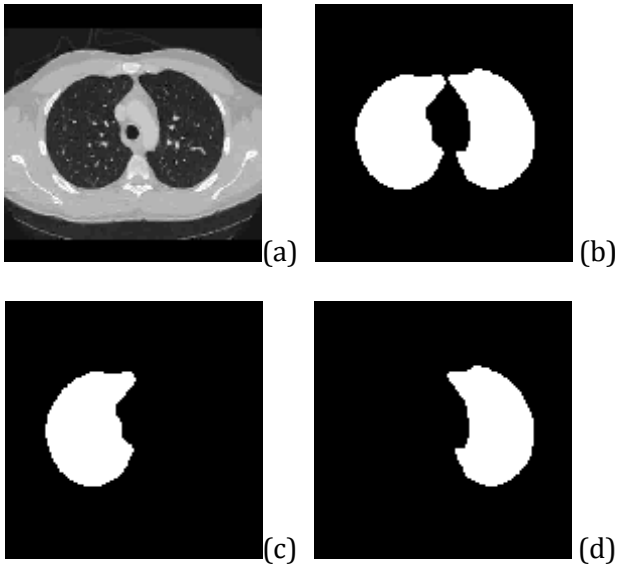

Figure 14 A CT image slice of the reference lung: (a) examination scan; (b) binary image of pulmonary region; (c) binary image of right lung and (d) binary image of left lung.

5.1.2 | CT Lung Segments Labelling

The bronchopulmonary segments were already defined in the anatomical atlas [8]. By stacking all slices, a 3D CT image of bronchopulmonary segments was created. The segment contours were resampled using the methodology already described for CT image of pulmonary region, producing a final 3D image with 64x64x64 voxels, where each bronchopulmonary segment consists in a set of voxels whose value is associated to the corresponding segment.

The terminology used for the bronchopulmonary segments was based on[8]. In order to facilitate the differentiation of each segment during the visualization, each voxel segment was labeled to values presented in table 4. According to the terminology, right lung consists of ten bronchopulmonary segments and left lung of eight. As in the 3D CT image of the pulmonary region, right and left lungs are also considered separately.

Table 4 Bronchopulmonary segments to right and left lungs and respectively voxel values

RIGHT LUNG	
Bronchopulmonary Segment	Voxel Values
Apical (SI)	10
Posterior (SII)	20
Anterior (SIII)	30
Lateral (SIV)	40
Medial (SV)	50
Superior (SVI)	60
Medial Basal (SVI)	70
Anterior Basal (SVIII)	80
Lateral Basal (SIX)	90
Posterior Basal (SX)	100

LEFT LUNG	
Bronchopulmonary Segment	Voxel Values
Apicoposterior (SI+II)	10
Anterior (SIII)	20
Superior Lingular (SIV)	40
Inferior Lingular (SV)	50
Superior (SVI)	60
Antero-Medial (SVII+SVIII)	70
Lateral Basal (SIX)	90
Posterior Basal (SX)	100

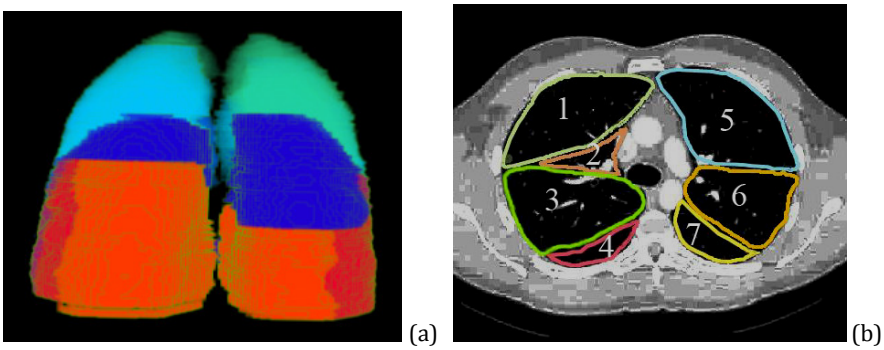

(a) (b)

Figure 15 (a) 3D CT image of bronchopulmonary segments. (b) CT image slice of the reference lung and respective bronchopulmonary segments (right lung: 1 - Anterior, 2 - Apical, 3 - Posterior and 4 - Superior; left lung: 5- Anterior, 6 - Apicoposterior and 7 - Superior)

5.2 | SPECT Images

The Nuclear Medicine Service of the Coimbra University Hospitals (NMS–CUH) acquired the ventilation and the perfusion SPECT scans used in this study. Following the methodology in[56], the NMS–CUH calculated the quotient SPECT images, the ventilation and perfusion binary images. Images from four patients with suspected pulmonary embolism were released to this study.

The SPECT scans were acquired by the following protocol: SPECT data were obtained from a Gamma Camera (Dual Head Millennium VG) in which the patient was in the supine position. The ventilation SPECT scans were acquired by inhalation of 37MBq of Technegas (an ultra-fine suspension of carbon nano-particles labeled with 99mTc). In the perfusion SPECT, the tracer used was the MAA (^{99m}Tc-Macroaggregates of Human Serium Albumin), which was administrated by intravenous injection. In a typical perfusion acquisition using this protocol, it is administrated 74 to 148 MBq of MAA. An

improvement in the detection of perfusion defects was achieved by using a higher activity and acquiring a perfusion scan after the ventilation scan. For both ventilation and perfusion SPECT acquisition was performed on Step and Shoot mode in a 180 degree orbit. The total acquisition duration for ventilation was 12 minutes and for perfusion 7 minutes. The matrix size for both ventilation and perfusion SPECT scans was 64x64 with 64 axial slices with 6.548x6.548x 6.548mm^3 of voxel dimensions.

After SPECT data acquisition, the hot spots were removed from the ventilation images. The hot spot are regions in image, with excess of counts and occur due to deposition of the tracer anywhere in the body, in this specific case the pulmonary region. By analyzing the histogram of the image, an expected maximum was found. The values that exceeded that maximum were resampled into a value range below it. Therefore, the hot spots were removed.

Since the perfusion scan was acquired immediately after the ventilation scan, the aerosol activity was also taken in account in the perfusion scan. To eliminate ventilation influence, a subtraction was done based on the following expression [56]:

$$C_p = C_{p+v} - kC_v \tag{2}$$

where C_p is perfusion count; C_v is ventilation count; C_{p+v} is perfusion count before the ventilation subtraction; k the decay factor.

To delineate the boundaries of the pulmonary region in the SPECT exam, the contour of the lungs was determined through a segmentation process. Obtaining a binary image allowed to identity right and left lungs and to remove extra pulmonary activity from trachea or stomach (the aerosol can in the end be swallowed when mixed with saliva during the ventilation acquisition). Image segmentation of ventilation and perfusion images was done by applying a threshold of 15% of the maximum calculated from the histogram of each image. After getting the lung contours, it was performed the normalization of the ventilation (after the hot spot removal) and perfusion (after subtraction of ventilation). By histogram analyzes, a normalization region was defined from a relative maximum. In the normalization region was considered 70% of the relative maximum for each ventilation and perfusion histograms. After normalization step, the quotient is determined by the following expression [56]:

$$Q_{VP} = n \times \frac{C_V}{C_P} \tag{3}$$

where n is the normalization factor.

During the registration process binary images of SPECT examinations of four patients were used. The pulmonary region was considered as a single area, since there might be areas that were not detected during the scan acquisition, the binary images of ventilation and perfusion of each patient were merged. As in CT images, the right and left lungs were separated and considered individually (Figure 16).

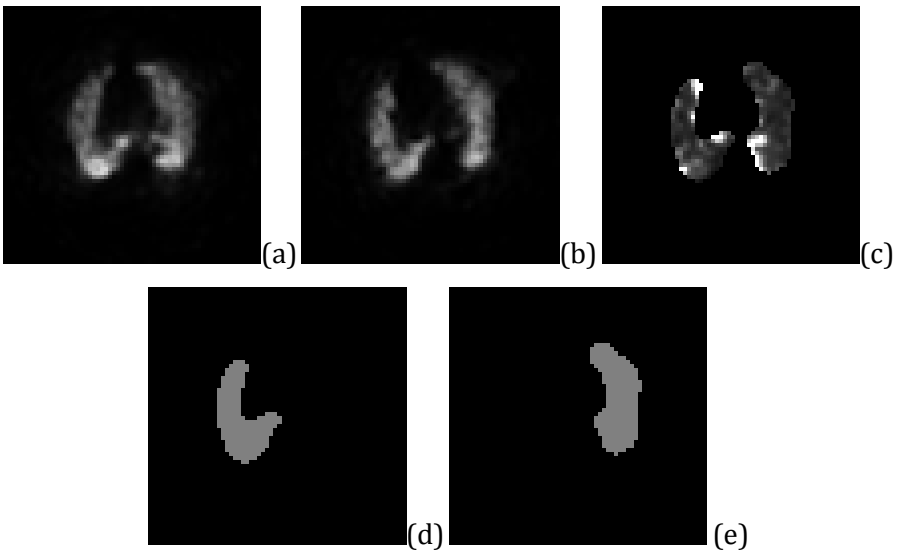

Figure 16 Patient A SPECT images of the same slice: (a) ventilation SPECT; (b) perfusion SPECT; (c) quotient SPECT; (d) binary image of right lung; and (e) binary image of left lung

5.3 | Registration

Image registration is a process that aligns two images, involving three main components: transformation, similarity metric and optimizer. The registration goal is changing the transformation parameters, using an optimizer, in order to find the optimal similarity metric value, which represents the quality of the alignment between the two images.

5.3.1 | Registration Transforms

The transformation functions define the set of operations that deforms the image to match another image. The image deformation is directly related to the degrees of freedom in which the transformation function is allowed to operate. In this work, it was used five transformation functions with different deformation characteristics: rigid (rigid body, global rescale, specific rescale and affine) and non-rigid (diffeomorphic demons).

5.3.1.1 | Rigid Transformation

The rigid transformation allows to move an object along an axis (translation), around a fixed axis (rotation); to enlarge or shrink an object by a scale factor (scaling) and to linearly deform an object along one axis (shearing). The transformations can be referred using homogeneous coordinates, that allows combining different transformations in a multiplication matrix form and therefore the computational method is simplified. The Following transformation matrices in homogeneous coordinates defines the translation (T), rotation (R), scaling (S) and shearing (Sh) over the x, y and z axes [11].

For translation in the x, y and z axes:

$$T = \begin{bmatrix} 1 & 0 & 0 & 0 \\ 0 & 1 & 0 & 0 \\ 0 & 0 & 1 & 0 \\ x & y & z & 1 \end{bmatrix}$$

where x, y and z represent the translation in each axis.

For rotation in the x, y and z axes:

$$R_x = \begin{bmatrix} 1 & 0 & 0 & 0 \\ 0 & \cos\theta_x & -\sin\theta_x & 0 \\ 0 & \sin\theta_x & \cos\theta_x & 0 \\ 0 & 0 & 0 & 1 \end{bmatrix}; R_y = \begin{bmatrix} \cos\theta_y & 0 & \sin\theta_y & 0 \\ 0 & 1 & 0 & 0 \\ -\sin\theta_y & 0 & \cos\theta_y & 0 \\ 0 & 0 & 0 & 1 \end{bmatrix};$$

$$R_z = \begin{bmatrix} \cos\theta_z & -\sin\theta_z & 0 & 0 \\ 0 & 1 & 0 & 0 \\ -\sin\theta_y & 0 & \cos\theta_y & 0 \\ 0 & 0 & 0 & 1 \end{bmatrix}$$

$$R = R_x \times R_y \times R_z$$

with θx, θy and θz represent the rotation angle in each axis. By multiplication the rotation matrixes for each axis, it is obtained a rotation global matrix.

For size scaling (S) in the x, y and z axes:

$$S = \begin{bmatrix} S_x & 0 & 0 & 0 \\ 0 & S_y & 0 & 0 \\ 0 & 0 & S_z & 0 \\ 0 & 0 & 0 & 1 \end{bmatrix}$$

where S_x, S_y and S_z represent the scale factor in each axis.

For shearing (Sh) in the planes xy, xz and yz:

$$Sh_x = \begin{bmatrix} 1 & Sh_{xy} & Sh_{xz} & 0 \\ 0 & 1 & 0 & 0 \\ 0 & 0 & 1 & 0 \\ 0 & 0 & 0 & 1 \end{bmatrix};\ Sh_y = \begin{bmatrix} 1 & 0 & 0 & 0 \\ Sh_{yx} & 1 & Sh_{yz} & 0 \\ 0 & 0 & 1 & 0 \\ 0 & 0 & 0 & 1 \end{bmatrix};\ Sh_z = \begin{bmatrix} 1 & 0 & 0 & 0 \\ 0 & 1 & 0 & 0 \\ Sh_{zx} & Sh_{zy} & 1 & 0 \\ 0 & 0 & 0 & 1 \end{bmatrix}$$

$$Sh = Sh_x \times Sh_y \times Sh_z$$

where $Sh_x, Sh_y\ and\ Sh_z$ represent the shear factor. By multiplication the shearing matrixes for each axis it is obtained a shearing global matrix. The global matrix of transformation is determined by multiplying the matrices of the parameters involved.

Rigid Body

A rigid body transformation is a rigid transformation that includes translations and rotations. In this registration distances and angles between points are preserved. A 3D rigid transformation allows six degrees of freedom which can be defined as translation in the x, y and z axes and rotations over the same axes. The translation and rotation matrices are multiplied and a global rigid body matrix (RB) is obtained:

$$RB = T \times R \tag{4}$$

Global Rescale

A global rescale transformation is similar to the rigid body transformation but also includes a uniform scaling factor along the x, y and z axis. This transformation allows preserving all angles and relative lengths in the transformed image. A 3D global rescale transformation has seven degrees of freedom which includes translations, rotations and a single scale parameter (S=Sx=Sy=Sz). All transformation matrices are multiplied and a global rescale matrix (GR) is obtained:

$$GR = T \times R \times S \tag{5}$$

Affine

An affine transformation allows preserving straightness of lines and parallel lines. However, the angles between the lines or planes are generally changed. A 3D affine transformation can have nine or twelve degrees of freedom. A nine parameter affine, which is called specific rescale transformation, allows translation, rotation and scaling over the x, y and z axes. All parameters matrices are multiplied and a global specific matrix is created (SR). A twelve parameter affine, which is only referred as affine, consists in translation, rotation, scaling and shearing operations over the x, y and z axes. All operation matrices are multiplied and a global affine matrix (A) is obtained.

$$\mathrm{SR} = \mathrm{T} \times \mathrm{R} \times \mathrm{S} \tag{6}$$

$$\mathrm{A} = \mathrm{T} \times \mathrm{R} \times \mathrm{Sh} \times \mathrm{S} \tag{7}$$

5.3.1.2 | Non-Rigid

Another category of registration algorithms is non-rigid transformations. The image is warped with non-linear transformations, allowing a smooth local variation and large deformations. The non-rigid algorithms can be defined as the transformation model, based on physical models. There are several models, with the elastic and fluid models being applied extensively. The elastic models are based on elastic mechanics and have a good performance when is needed small deformations. The fluid model is based on the equations of fluid dynamics and it is usually applied in large deformations [57].

In this study, the diffeomorphic demons transformation was used. This registration algorithm used a transformation which belongs to a group of diffeomorphism Diff(Ω) and it is represented as the composition of the following expression [54]:

$$\varphi = \psi \circ Exp(u) \tag{8}$$

where φ is an element in $Diff(\Omega)$ and u is a vector field in Ω belonging to a convenient space vector fields that guarantees the existence of the exponential map and the composition $\psi \circ Exp(u)$ remains in $Diff(\Omega)$. This characterization restricts transformations to any element in $Diff(\Omega)$ that can be obtained by finite composition of exponential of smooth vector fields [54]:

$$\varphi = Exp(u_1) \circ \ldots \circ Exp(u_N) \tag{9}$$

5.3.2 | Similarity Metrics

A similarity metric measures the differences between two images. The optimal value is achieved when the images are completely coincident. During the registration method, iterative calculations are done between the moving image and reference image, until an optimal value is reached. The following metrics were used in the registration methods: Normalize Cross Correlation and Normalized Mutual Information.

Normalized Cross Correlation:

The Normalize Cross Correlation (NCC) has an intrinsic characteristic, considering that the corresponding intensities in two images have a linear correlation [46]. This metric multiples the intensity of two images in each voxel, sums the obtained product and divides it by the square root of the multiplication of the intensity squared. The resulting values are between zero and one. The one value means that the images are totally coincident and zero value means no linear relationship, i.e., images are totally different.

$$NCC = \frac{\sum_x^I \sum_y^J \sum_z^K A(x,y,z) \times B(x,y,z)}{\sqrt{\sum_x^I \sum_y^J \sum_z^K A(x,y,z)^2 \times \sum_x^I \sum_y^J \sum_z^K B(x,y,z)^2}} \quad (10)$$

where A and B are both images; x, y and z are the coordinates on the images; and X, Y and Z the dimensions of the images.

Normalized Mutual Information

The Normalized Mutual Information (NMI) is related to the statistical dependence between the intensity of two images [46]. This metric is proportional to the entropy of the image A and B, divided by the joint entropy H (A, B). The resulting values are between zero and one. On the one hand, NMI value is zero the images are very different; on the other hand, NMI is 1 the images are perfect identical.

$$NMI = \frac{H(A)+H(B)}{H(A,B)} \quad (11)$$

$$\mathrm{H(A)} = -\sum_{a \in A} \mathrm{p(a)} \log \mathrm{p(a)} \,;\, \mathrm{H(B)} = -\sum_{b \in B} \mathrm{p(b)} \log \mathrm{p(b)} \,;$$

$$\mathrm{H(A,B)} = -\sum_{a \in A} \sum_{b \in B} \mathrm{p(a,b)} \log \mathrm{p(a,b)}$$

where H (A) is the entropy of the image A; H (B) the entropy of image B; H (A, B) the joint entropy of image A and B; p (a) is the probability of image A; p (b) is the probability of image B and p (a, b) joint probability of image A and B.

5.3.3 | Optimization and Registration Algorithms

An optimizer defines how the transformation parameters are modified to optimize the similarity metric. A good optimizer is the one that, in a few iterations, locates the best possible transformation parameters in which the metric value is closer to its optimal value. The optimization of rigid registration was based on Powell's algorithm [58]. It is a nonlinear optimizer that iteratively varies each transformation parameter in turn, in order to achieve the optimal value of the similarity metric. In non-rigid registration was applied an iterative optimization based on Lei groups [54].

Rigid algorithm

The registration method applied is based on a multi-resolution approach, which is initialized in a low resolution and iteratively increases the resolution as the optimal value of the similarity metric is determined, for each resolution level. By applying lower resolutions in the initial iterations, it is allowed an alignment with few points, which reduces the computational cost.

The registration algorithm started with a pre-optimization step, in which both reference and moving image were interpolated by a trilinear algorithm[8] to create isotropic voxel image (used in level-1 optimization)and to resampled the image size to 4 and 2 times smaller (used in level-4 and level-2 optimizations, respectively). For the 4 downsampled reference and moving images, the centers of mass of each image were calculated by relating the position and pixel area. Afterward, a translation was applied to align the centers of mass. Then, the transformation parameters were adjusted by the optimizer to search for the metric optimal value. The parameters determined on the previous step were used as initial transformations on the level-2 optimization. The same procedure was repeated to level-1 optimization. By applying the trilinear interpolation and the parameters calculated in the level-1 optimization, the moving image was transformed into the same coordinate system as the reference image, and a transformation matrix was obtained.

[8]Trilinear interpolation computes values based on 8-neighborhood connection.

Diffeomorphic Demons algorithm

In this work was used a diffeomorphic demons registration algorithm based on[54] to search the transformation parameters that maximize an energy. The energy consisted of the similarity metric and a regularization term.

The method was initialized by an estimation of an initial transformation by a mapping point. In each iteration, the displacement field (speed vector field) was updated by a composite adjustment. Updating search was done using a Lie group structure, in which an exponential mapping was defined from the vector space of velocity fields into the diffeomorphic space. A local estimation might cause inconsistency between neighbor voxels, which could generate instability and loss of continuity in the region of interest. To solve this problem, a regularization step was applied by using a Gaussian convolution kernel to the speed vector field in order to smooth and kept the image continuity. In each iteration, the moving image is deformed using the updated and regulated deformation field. The speed vector field was estimated until was achieved the convergence of the energy. At the end of the iterative alignment, a transformation matrix was obtained.

6 | Results and Discussion

To identify the pulmonary regions in lung SPECT scans with suspicion of pathology, a study of registration algorithms was performed. A pre-processing step was done to obtain the binary images of CT scan, the ventilation and perfusion SPECT scans. Then, by applying five different registration algorithms and comparing their performance, the best of algorithm was selected. The transformation matrix of the best algorithm was applied to the SPECT scans and comparing with the CT image and the segments with suspicion of pathology were indentified.

In this chapter, it is shown the results obtained with the proposed methodology. First, the segmentation of the pulmonary region and bronchopulmonary segments are examined. Then, performance of the registration algorithms are analyzed using the processing time, the overlay between the aligned images and the reference image, and comparing the similarity metric values. Finally, by visual comparison, the suspected pathologic segments are identified.

The following software was used: Matlab [59] (segmentation of pulmonary region in CT scan); MIPAV [53] (registration process) and Rview [60] (visualization and overlay).

The images had 64x64x64 voxels and the following orientation: right to left in x-axis, anterior to posterior in y-axis and superior to inferior in z-axis (Figure 17). All methodologies were computed on a laptop with Intel Pentium M processor 2.00GHz with 1.00GB of RAM, running Windows XP operating system. The right and left lungs were analyzed individually.

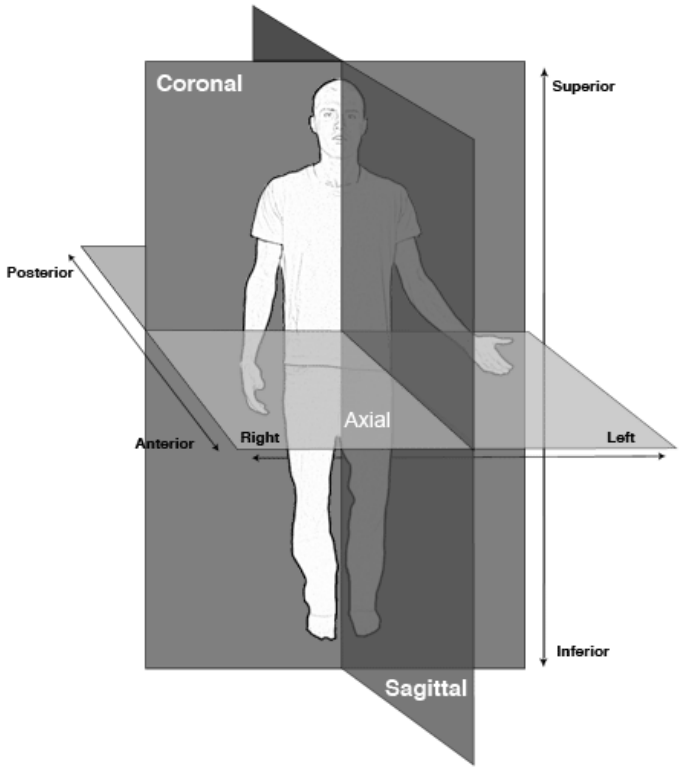

Figure 17 Anatomical planes [61]

6.1 | CT Segmentation

A lung segmentation procedure was used to create 3D binary images, used by the multimodality registration process. In this section is presented the visual inspection analysis that was performed in 3D CT images of the pulmonary region and bronchopulmonary segments.

6.1.1 | Pulmonary Region

In order to create a binary image of the pulmonary region of the reference CT scan, the segmentation methodology described in 5.1.1 was applied. A radiologist expert performed a qualitative analysis of the results by visual inspection and verified that the binary masks are correct borders of the entire lung. In figure 18(a) it is shown the overlay of the CT scan with the binary masks of the right (red) and left (green) lungs in the axial, coronal and sagittal perspectives. The figure 18(b) is a three-dimensional representation of the overlay of the thoracic region.

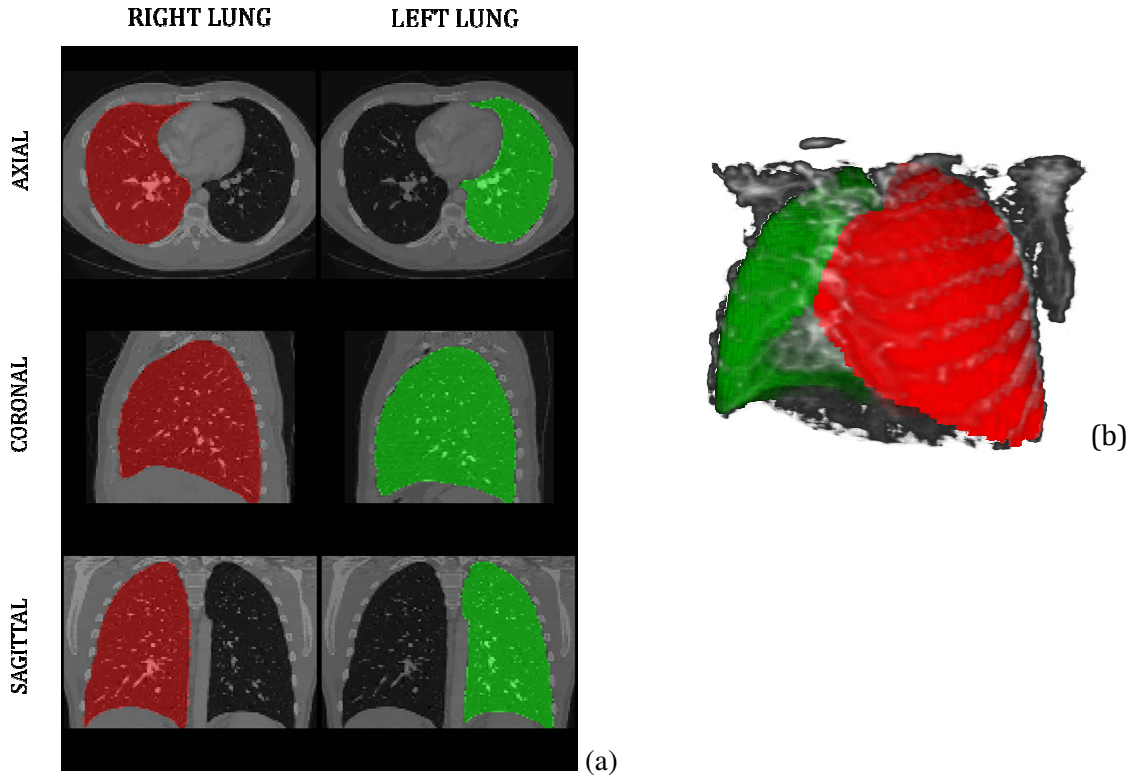

Figure 18 Overlay between CT binary masks and CT scan of a reference lung in (a) axial, coronal and sagittal perspectives; and a three-dimensional representation. Right lung is in red and left lung in green.

6.1.2 | CT Bronchopulmonary Segments

The bronchopulmonary segments were defined using the method described in section 5.1.2. The same radiologist expert performed a qualitative analysis of the binary masks of each lung segment and verified that the bronchopulmonary segments were well aligned with the pulmonary region of the CT scan and any overlap between the different lung segments detected, was immediately corrected. In figure 19(a) is represented the overlay between the CT scan and the bronchopulmonary segments of the right and left lungs in the axial, coronal and sagittal perspectives. Each lung segment was labeled with a value, which corresponds to a different color when visualized. Figure 19(b) represents a three-dimensional representation of the CT scan of the reference lung in which a region was removed to be able to observe the details of right lung interior with the bronchopulmonary segments.

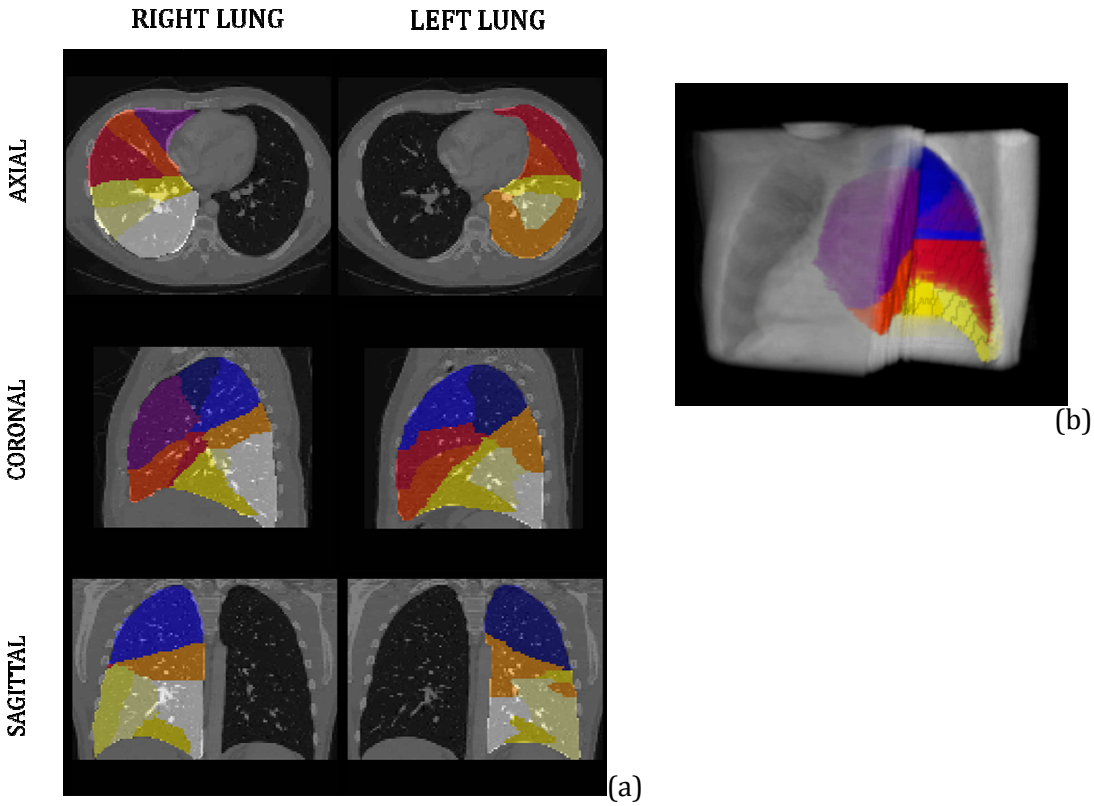

Figure 19 Overlay between CT binary masks of bronchopulmonary segments and CT scan of a reference lung in (a) axial, coronal and sagittal perspectives; and in a three-dimensional representation. Each bronchopulmonary segment is associated with a different color.

6.2 | Registration

To proceed with the registration, four rigid algorithms with six (rigid body), seven (global rescale), nine (specific rescale) and twelve (affine) degrees of freedom and a non-rigid algorithm (diffeomorphic demons) were applied to evaluate their influence in the evolution of the alignment of 3D CT and SPECT binary images to selected the algorithm that have a better performance in a relation alignment /processing time to be used in the identification of suspected pathological regions.

6.2.1 | Processing Time

For each registration process of the eight lungs (right and left lungs of four patients) using different transformation algorithms (rigid body, global rescale, specific rescale, and diffeomorphic demons), the processing time was measured (Figure 20 and Table 5). Rigid registration was the fastest algorithm taking about 20 seconds, and the longer algorithm was diffeomorphic demons taking about 130s, i.e., 2 minutes and 10 seconds.

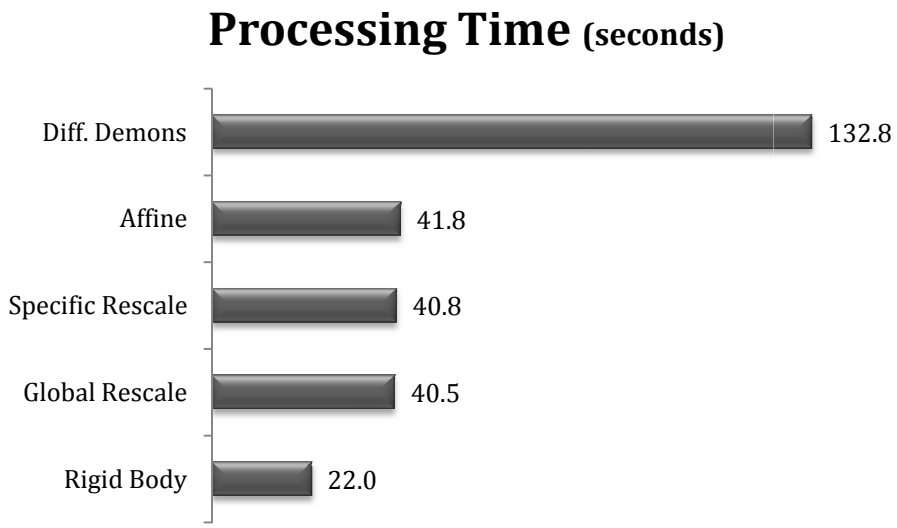

Figure 20 Mean processing time for each registration algorithm

Table 5 Processing time of each registration algorithm

TRANSFORMATION	PATIENTS							
	RIGHT LUNG				LEFT LUNG			
	Patient A	Patient B	Patient C	Patient D	Patient A	Patient B	Patient C	Patient D
Rigid Body	19.7	22.7	22.8	22.1	22.6	23.4	20.4	24.0
Global Rescale	38.7	45.2	37.4	42.7	38.8	41.7	36.8	38.8
Specific Rescale	39.1	46.0	38.0	43.4	39.5	41.6	37.4	38.9
Affine	40.2	47.6	39.2	44.4	40.5	42.7	38.3	41.3
Diff. Demons	127.3	129.5	131.3	130.1	126.5	153.1	130.9	134.1

These results show that increasing the transformation complexity also increases the processing time.

6.2.2 | Overlay between reference image and moving image

The performance of a registration process was evaluated in terms of overlay between the reference image and the moving image after registration. By visual inspection a qualitative analysis was done of the overlay before registration process and after being processed by each transformation algorithm. Also in this analysis it was counted the number of voxels and computed the absolute and relative errors.

6.2.2.1 | Qualitative analysis

To be presented here, two SPECT images were randomly selected. The visual overlay were computed between binary mask of the pulmonary region of the CT scan (gray) and binary mask of SPECT (ventilation and perfusion) before registration (green) and after registration: rigid body (red), global rescale (blue), specific rescale (yellow), affine (brown) and diffeomorphic demons (pink) (Figures 21 and 22).

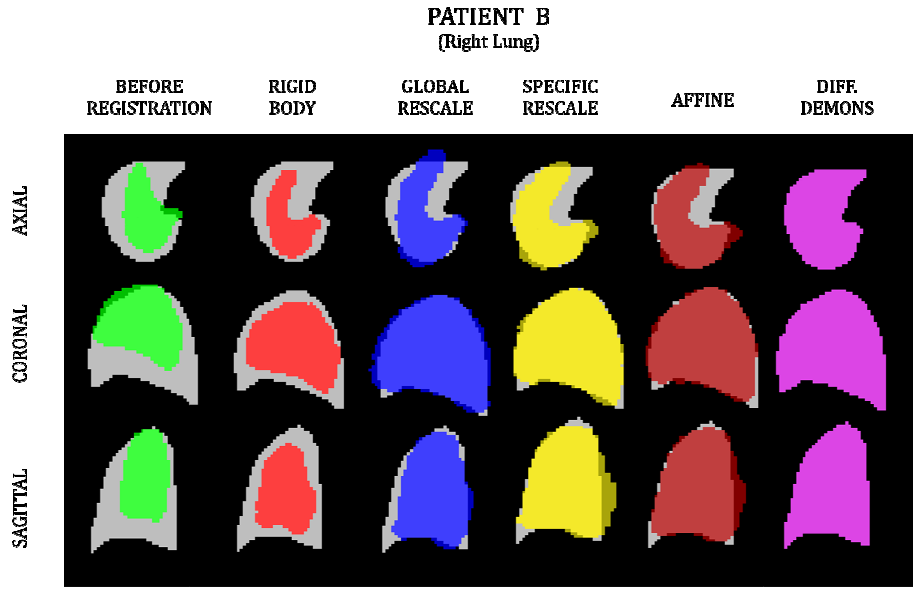

Figure 21 Overlay of reference image (gray) and moving image of patient B (right lung) before registration process (green) and after registration: rigid body algorithm (red), global rescale (blue), specific rescale (yellow), affine (brown) and diffeomorphic demons (pink).

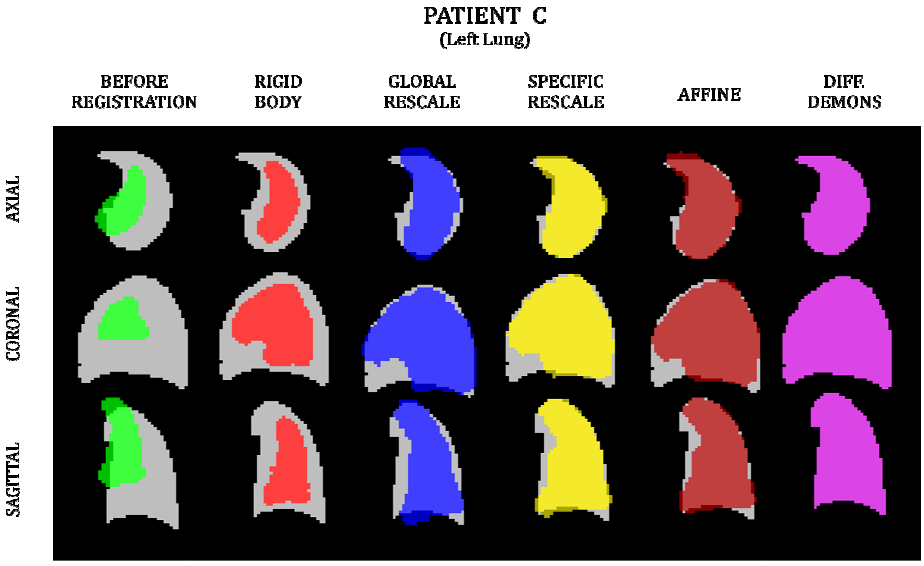

Figure 22 Overlay of reference image (gray) and moving image of patient C (left lung) before registration process (green) and after registration: rigid body algorithm (red), global rescale (blue), specific rescale (yellow), affine (brown) and diffeomorphic demons (pink).

Before registration process, the misalignment between the two binary images was observed. The rigid body registration shows that the moving image was centered in the CT binary image. By increasing the complexity with the scaling transformation in case of the global rescale, specific rescale and affine, in which in addition to scaling had shearing, the SPECT (ventilation and perfusion) binary mask had a better fit to the image, comparatively to rigid body registration process. With diffeomorphic demons algorithm was obtained an almost perfect alignment, with a complete overlay of the reference and moving binary images.

6.2.2.2 | Calculation of the absolute and relative errors

The overlay between the registered image and the reference image can be analyzed in terms of voxels computed from the histogram.Therefore, the CT binary image (which had the voxel value "1" for lung region and the voxel value "0" for non lung region) was added to the SPECT binary image (which was multiplied by two so that the lung voxel value would have "2") (Figure 23). Thus, the sum of the two images corresponds to an overlay; computing its histogram, it was obtained the number of voxels that belong to the overlaying of CT and SPECT binary images.

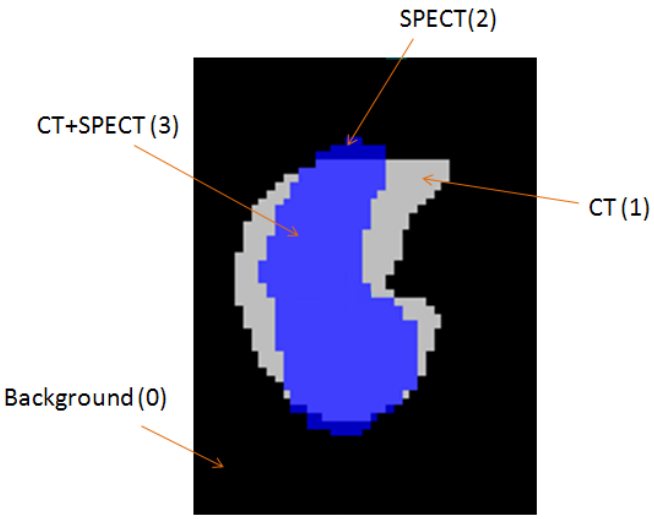

Figure 23 An overlay image showing the voxel values

Besides the number of voxels, was also determined the absolute error and relative error using the following expressions:

$$Absolute\ Error = \big(CT - (CT + SPECT)\big) + \big(SPECT - (CT + SPECT)\big) \quad (12)$$

$$Relative\ error = \frac{CT-(CT+SPECT)}{CT} \times 100 \quad (13)$$

where CT is the total number of voxels of CT image, SPECT is the total number of voxel of SPECT image and (CT + SPECT) is the total number of voxels in common of CT and SPECT images. The addition between CT and SPECT voxels represents logic AND, which is the common region of the two images. Since CT image was the reference image during the registration process, its number of voxels could be represented as a target value, i.e., the theoretical value of the alignment. Thus, the practical approximation value obtained in each registration process is (CT + SPECT). The absolute error is the total number of voxels of CT image $\big(\text{CT} - (\text{CT} + \text{SPECT})\big)$ and SPECT image $(\text{SPECT} - (\text{CT} + \text{SPECT}))$ which do not belong to the overlay. By analogy, the absolute error represents the difference between the theoretical value of CT and practical value of the overlay (CT + SPECT).The relative error represents the deviation between the number of voxels of CT image (target value) and the number of voxels of the overlay (CT + SPECT). The smaller the absolute and relative error, the best is the alignment between the reference and the moving images. By analyzing the results of table 6 to a random patient, it is observed that with increasing algorithm complexity, the errors decrease, which means better fit between the two images.

Table 6 Overlay analysis: absolute and relative errors

	PULMONARY REGION (PATIENT C – Right Lung)				
	Number of Voxels			**Absolute Error**	**Relative Error**
	CT	SPECT	CT+SPECT		
Before Registration	20054	3948	3808	16386	81.0%
Rigid Body	20054	6288	6287	13768	68.6%
Global Rescale	20054	17133	14749	7689	26.5%
Specific Rescale	20054	19224	17489	4300	12.8%
Affine	20054	19056	17494	4122	12.8%
Diff. Demons	20054	20018	19985	102	0.3%

In table 7, it is a summary of the obtained results from the relative errors of the eight lungs in the five registration algorithms. Before registration process was observed that the eight lungs had a relative error between 80% and 88%. By applying the rigid body algorithm was achieved a relative error between 63-77%. With global and specific Rescale, the relative error significantly decreases varying between 18-36% and 13-25%,

respectively. With affine transformation was obtained relative errors below 20%. The best alignment was obtained with the diffeomorphic demons algorithm, in which was achieve relative errors below 1%. This means that 99% of SPECT image was overlaying the CT image (Figure 24).

Table 7 Summary of the relative errors of each registration process for the right (RL) and left (LL) lungs of the four patients

PATIENTS	Before Registration Process	Rigid Body	Global Rescale	Specific Rescale	Affine	Diff. Demons
Patient A (RL)	79.5%	63.3%	27.1%	13.5%	13.5%	0.9%
Patient A (LL)	84.0%	68.5%	36.3%	25.1%	19.7%	0.3%
Patient B (RL)	78.4%	63.7%	26.9%	20.2%	19.5%	0.1%
Patient B (LL)	78.0%	57.9%	25.1%	16.3%	14.1%	0.1%
Patient C (RL)	81.0%	68.6%	26.5%	12.8%	12.8%	0.3%
Patient C (LL)	84.7%	67.7%	23.2%	17.0%	15.4%	0.2%
Patient D (RL)	85.5%	73.2%	17.7%	15.7%	13.2%	0.3%
Patient D (LL)	87.8%	77.1%	21.2%	19.1%	18.6%	0.2%

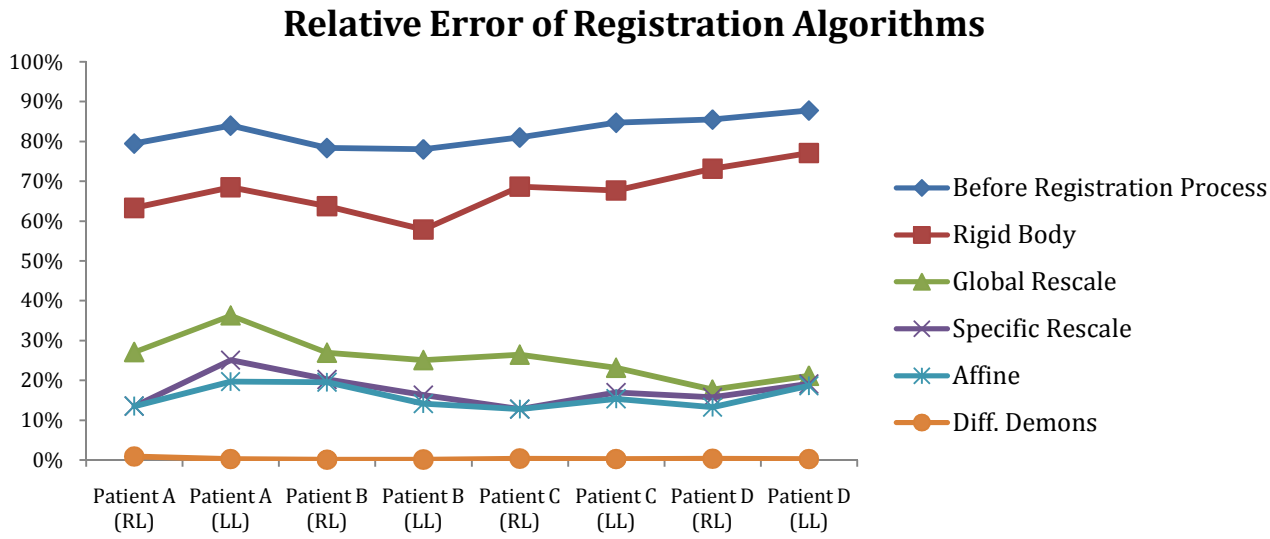

Figure 24 Relative error of each registration process

6.2.3 | Similarity Measure

The similarity metric reflects the likeness between the reference image and the moving image in a registration process. Two similarity metrics were used: Normalized Cross Correlation (NCC) and Normalized Mutual Information (NMI).

NCC varies between 0 and 1 values, in which "0" value corresponds to different images and "1" value to identical images. NMI varies in a range of 0 to 1, in which the "0" value corresponds to different images and "1" value to identical images. In tables 8 and 9 is presented the obtained results of the two metrics in the five registration algorithms of the eight studied lungs. The rigid body algorithm had relatively low values for the similarity metric, which means that the images showed little resemblance. For NCC the metric values were about 0.6 and 0.3 for the NMI. By increasing the complexity of the transformation on global rescale, specific rescale and affine algorithms, occurs a significant increasing on similarity values, in which it was observed an approach of the optimal value of the metric. The diffeomorphic demons algorithm performed the best alignment, in which both metrics are close to 1, which means that the moving image (SPECT binary image) is identical to the reference image (CT binary image).

Table 8 NCC similarity values of each registration process

	RIGID BODY	GLOBAL RESCALE	SPECIFIC RESCALE	AFFINE	DIFF. DEMONS
Patient A (RL)	0.588	0.790	0.872	0.877	0.995
Patient A (LL)	0.546	0.724	0.806	0.836	0.998
Patient B (RL)	0.585	0.791	0.829	0.842	0.999
Patient B (LL)	0.634	0.796	0.854	0.866	0.999
Patient C (RL)	0.543	0.778	0.881	0.885	0.997
Patient C (LL)	0.553	0.813	0.859	0.864	0.999
Patient D (RL)	0.501	0.834	0.859	0.881	0.998
Patient D (LL)	0.464	0.826	0.835	0.839	0.999

Table 9 NMI similarity values of each registration process

	RIGID BODY	GLOBAL RESCALE	SPECIFIC RESCALE	AFFINE	DIFF. DEMONS
Patient A (RL)	0.386	0.586	0.708	0.718	0.98
Patient A (LL)	0.344	0.502	0.612	0.654	0.992
Patient B (RL)	0.382	0.586	0.640	0.662	0.998
Patient B (LL)	0.438	0.594	0.682	0.700	0.996
Patient C (RL)	0.338	0.566	0.722	0.732	0.988
Patient C (LL)	0.350	0.620	0.692	0.698	0.994
Patient D (RL)	0.296	0.644	0.686	0.724	0.992
Patient D (LL)	0.262	0.64	0.650	0.658	0.994

The box plot analysis allows to observe the data distribution of each registration algorithm using the two similarity metrics (Figure 25). A box plot is defined by the median, upper and lower quartiles, and maximum and minimum data values. The median is the value that divides the data into two halves. The position of the median in the box is related to the data symmetry. The upper quartile indicates that 25% of data is greater than this value and the lower quartile defines that 25% of data is lower. The up end of the whisker is the maximum, which is the greater value and the down end of the whisker is the minimum, which is the lower value. Considering the whiskers limited between 1.5 times of the inter-quartile range, the outliers will be defined as all the values that do not fit in this interval [62]. To perform the box plot chart was used the Statistics Toolbox™ of Matlab [63]**.**

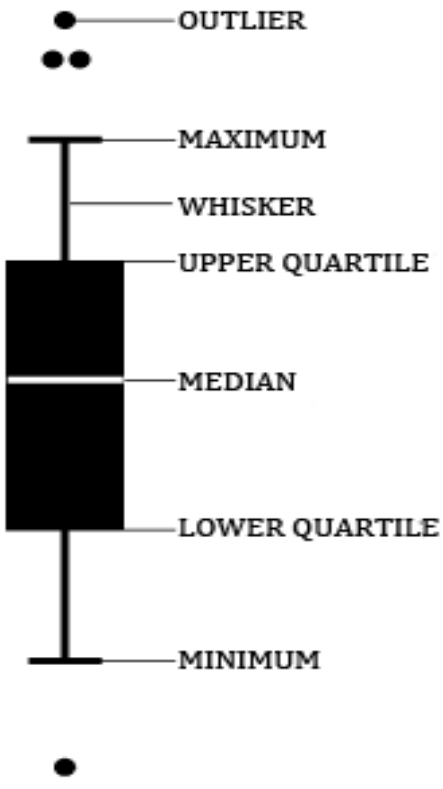

Figure 25 Box plot interpretation

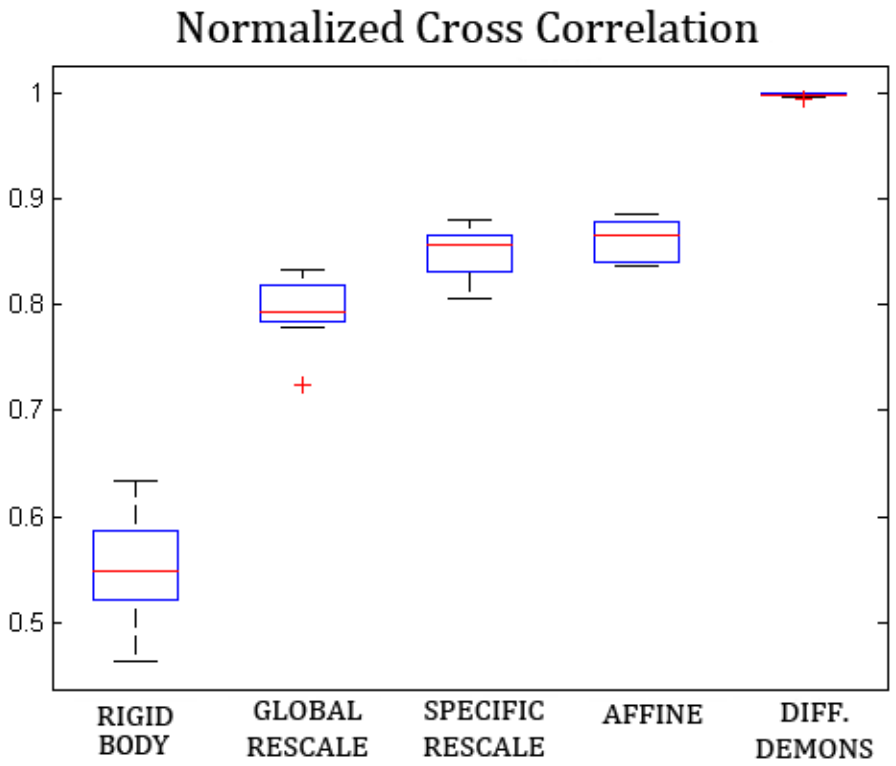

Figure 26 NCC box plot chart for each registration process

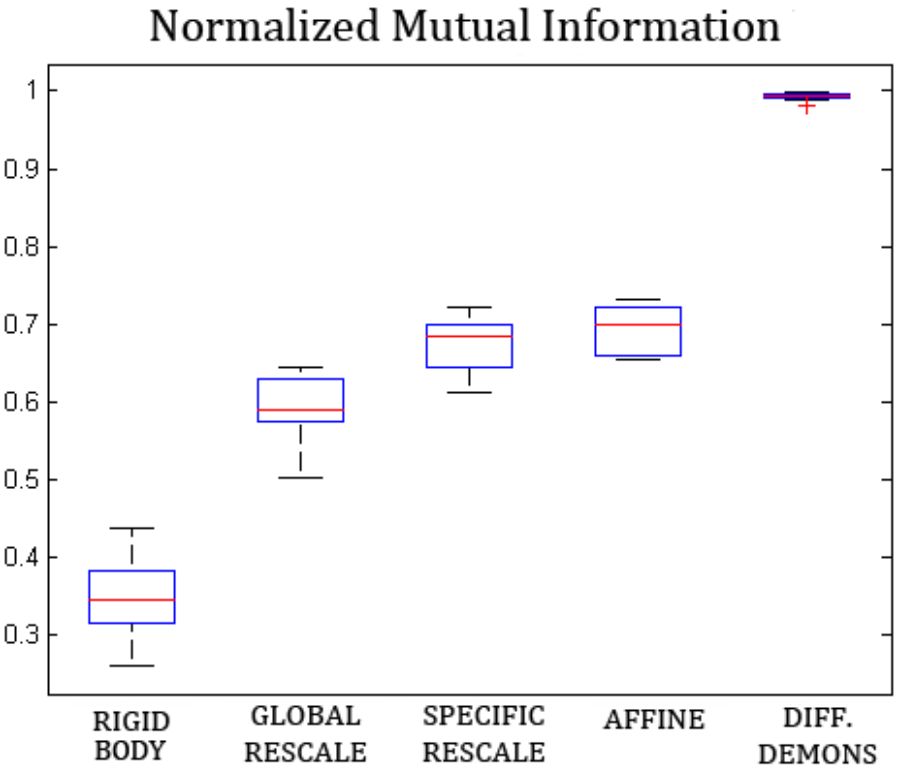

Figure 27 NMI box plot chart for each registration process

In figures 26 and 27, comparing the distances between the maximum and minimum values to the upper quartile and lower quartile, respectively, i.e., the length of whiskers, it was observed that the rigid body registration has the highest dispersion data and the diffeomorphic demons the lowest. By decreasing the distance between the upper and lower quartiles, consequently the uniformity of data increases. For both metrics, there is an increasing in the data consistency with the increasing of the complexity of the registration algorithms. Therefore, since the median is higher in the diffeomorphic demons transformation, this registration algorithm achieves the best alignment.

6.3 | Identification of Regions with Suspected Pulmonary Embolism

From the registration process, a transformation matrix was obtained and applied to the three SPECT images (ventilation and perfusion examinations and quotient image) resulting in an alignment between the three SPECT images and the SPECT binary image, which in turn was aligned with the binary CT image of the pulmonary region. With this process, all images were aligned to the CT image of the bronchopulmonary segments. Therefore, by visual comparison between the SPECT scans and the CT image of the lung segments, it was possible to identify the location of the bronchopulmonary segments in the SPECT scans.

Despite the best registration performance was obtained by the diffeomorphic demons algorithm, its elastic behavior can compromise the identification of the suspected pathologic regions; since this algorithm applies a distortion to achieve a perfect alignment, data information can be distorted and missing lung regions that might be pathologic. Hence, affine transformations were used to the identification, once that have a high degree of freedom but without deformation. Affine registration also combines a good alignment in a low processing time.

In a normal lung SPECT examination, ventilation is similar to perfusion, i.e., the number of counts of the two examinations is very similar, which is reflected in a visual similarity between the two exams. Ventilation SPECT may have low counts due to incorrect aerosol inhalation or airway obstruction. Also it can be detected, both in ventilation and perfusion, an excess of counts derived from tracer deposition. In a case of a patient with suspected pulmonary embolism, there is a mismatch between

ventilation and perfusion counts, with a higher number of counts in ventilation. This mismatch results in an impact on the quotient image.

One patient was randomly chosen and the SPECT images of this patient were included in this thesis (Figure 28). By visual inspection of these exams, a mismatch activity was detected between ventilation and perfusion SPECT scans (marked areas), where ventilation exam has higher number of counts when compared with the perfusion scan. Consequently, the quotient SPECT image has more intense activity in those areas (lighter area). By comparing with the CT image of bronchopulmonary segments, it was observed that mismatch areas were in Posterior Basal segment (dark red segment in CT image).

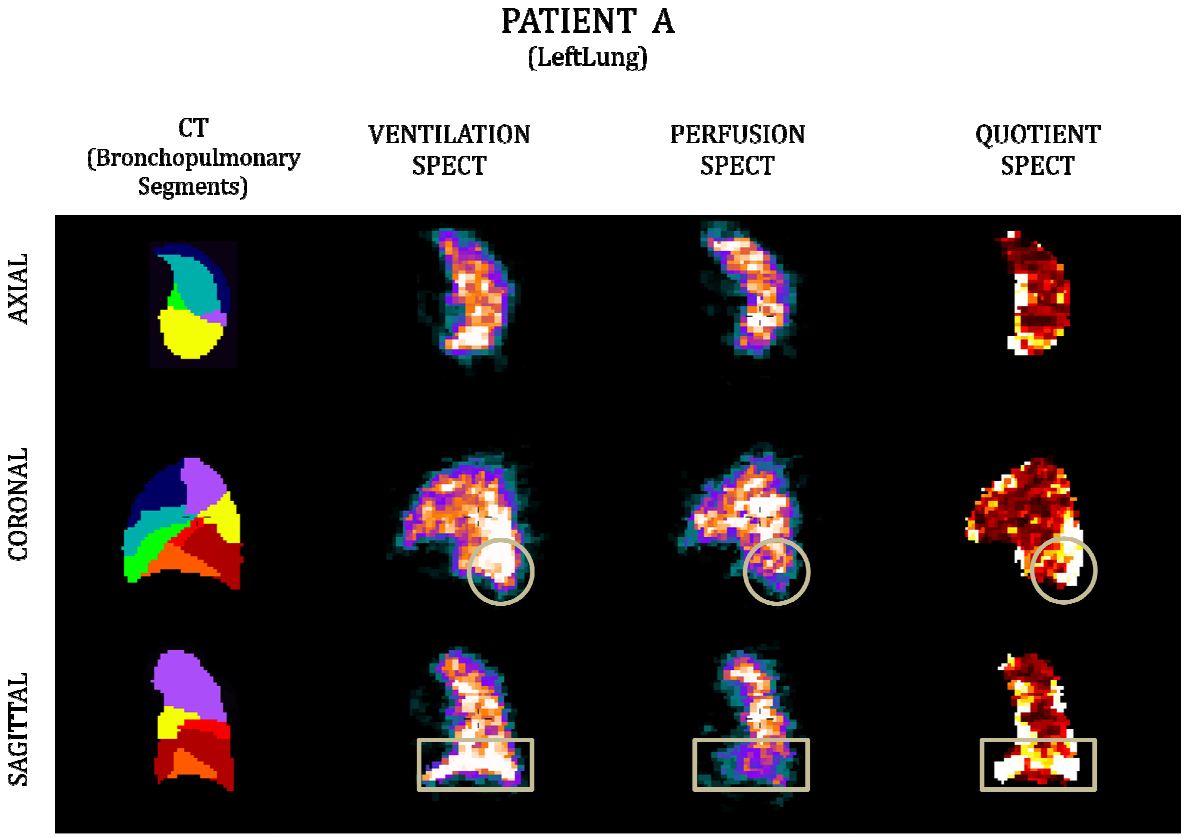

Figure 28 Mismatch between ventilation and perfusion SPECT scans and identification of the bronchopulmonary segment

These results were shown to an expert physician, who confirm the suspicion of pathologic pulmonary region and classified this methodology as a good clinical tool to support medical analysis in a diagnosis context.

7 | Conclusions and Future Work

Imagiologic techniques may be useful tools to assist the medical diagnostic, helping the physician in a fast identification of pathologic lung regions. In the case of pulmonary embolism, ventilation and perfusion SPECT scans are acquired and often combined with CT scans. Through the application of this multi-modality registration, two exams from different imagiologic modalities can be aligned and compared to improve the diagnosis.

In this thesis, it is performed the study of registration methods, aiming the identification of bronchopulmonary segments affected by pulmonary embolism. The proposed methodology starts with the extraction of pulmonary region from the 3D CT scan of a reference lung and a contour definition of the bronchopulmonary segments. Using the binary pulmonary images of SPECT scans, an alignment was done between these images and the CT binary image of pulmonary region. Then, in the registration step, five transformation algorithms (rigid body, global rescale, specific rescale, affine and diffeomorphic demons) were analyzed in order to select the best algorithm in terms of alignment and processing time. Although diffeomorphic demons algorithm achieved the best alignment (i.e., closer to the optimal similarity value) its computational efficiency is low taking a long time to do the image processing. The present work suggests that the segments could be preferable identified using affine transformation due to their low processing time and relatively good registration results.

In conclusion, the results obtained in this study showed that the application of multimodality registration has a relevant role in the identification of suspected pathological pulmonary regions, therefore being a promising tool for medical diagnostic.

7.1 | Future Work

As future work, the application of the proposed methodology will use higher resolution images to increase the quality of the image and, thereby improve the performance in the identification of lung regions. Due to high variability in shape and size of the lungs, it is necessary to expand the study to a larger number of patients to have a broader perspective of the applicability of the methodology. The identification of bronchopulmonary segments will be extended from visual inspection to a quantitative analysis approach. To validate the results, a statistical analysis comparing the results calculated by a voxel to voxel comparison between CT and SPECT images and the results produced by physicians for the same examinations.

Bibliography

[1] Alvares F., et. al., *Tromboembolismo pulmonar: diagnóstico e tratamento,* Simpósio: Urgências e Emergências Respiratórias, vol. 36, pp. 214-240, 2003.

[2] Wrong Diagnosis. (2010, July 28). *Statistics by Country for Pulmonary Embolism*. Available: http://www.wrongdiagnosis.com/p/pulmonary_embolism/stats-country.htm

[3] Blachere H., et al., *Pulmonary embolism revealed on helical CT angiography: comparison with ventilation-perfusion radionuclide lung scanning*, AJR Am J Roentgenol, vol. 174, pp. 1041-7, 2000.

[4] Abrantes L. B., et. al., *Multimodality Segmentation and Registration of 3D Pulmonary Exams*, 5th Iberian Conference in Systems and Information Technologies (CISTI 2010) IEEE conference, vol. 2, pp. 89 – 92, 2010.

[5] Mader S. S., *Understanding Human Anatomy & Physiology*, Fiftth Edition ed.: The McGraw-Hill Companies, 2004.

[6] Virtual Medical Center. (2010, August 2). *Pulmonary Embolism*. Available: http://www.virtualmedicalcentre.com

[7] (2010, August 15). *Human Respiration*. Available: http://www.goldiesroom.org/Note%20Packets/13%20Human%20Other/00%20Human%20Other%20Systems--WHOLE.htm

[8] IMAIOS. (2009, October 2). *Human anatomy: medical imaging and illustrations*. Available: http://www.imaios.com/en/e-Anatomy

[9] Stein P. D., et. al. *Acute pulmonary embolism*, Curr Probl Cardiol, vol. 35, pp. 314-76, 2010.

[10] Vascular Society of Egypt. (2010, August 15). *Pulmonary Embolism*. Available: http://www.vsegypt.org/index.php/vascular-surgery-cme/articles/39-pulmonary-embolism-.html

[11] Jan J., *Medical Image Processing, Reconstruction and Restoration*: Taylor & Francis Group, 2006.

[12] Hsieh J., *Computed Tomography: Principles, Design, Artifacts, and Recent Advances*, Spie Press, 2003.

[13] Imaginis. (2010, June 29). *Brief History of CT*. Available: http://www.imaginis.com/ct-scan/brief-history-of-ct

[14] Suetens P., *Fundamentals of Medical Imaging*, Second Edition ed.: Cambridge University Press, 2009.

[15] (2010, July 28). *Computed Tomography Imaging*. Available: http://belley.org/ct/ct/index.htm

[16] Radiology-. Equipment.com. (2010, June 29). *Toshiba Asteion - Helical CT Scanner*. Available: http://www.mri-equipment.com/detail.CFM?LineItemID=1237

[17] Bushberg J. T., *The Essential Physics of Medical Imaging*, Second Edition ed.: Lippincott Williams & Wilkins, 2002.

[18] Medical Diagnostics - GE Healthcare. (2010, June 30). *Modalities and methods: Computed tomograpy*. Available: http://www.medcyclopaedia.com/library/radiology/chapter04/4_2.aspx

[19] UNSCEAR. (2010, June 30). *Report of the United Nations Scientific Committee on the Effects of Atomic Radiation to the General Assembly*. Available: http://www.unscear.org/docs/reports/gareport.pdf

[20] American College of Radiology and Radiological Society of North America. (2010, June 30). *The Radiology Information Resource for Patients*. Available: www.radiologyinfo.org

[21] eHealthMD. (2010, June 30). *When Is A Contrast Agent Required?* Available: http://www.ehealthmd.com/library/ctscan/CTS_contrast.html

[22] Wernick, M. N., *Emission Tomography: The Fundamentals of PET and SPECT*: Elsevier Academic Press, 2004.

[23] Medical Diagnostics - GE Healthcare. (2010, June 30). *Physics, Techniques and Procedures: Pet imaging*. Available: http://www.medcyclopaedia.com/library/topics/volume_i/p/pet_imaging.aspx

[24] Berkeley Lab. (2010, June 28). Available: http://www.lbl.gov/images/PID/Hal-Anger.jpg

[25] Israel O., *Hybrid SPECT/CT Imaging in Clinical Practice*: Taylor & Francis Group, 2006.

[26] Glasgow Experimental MRI Center. (2010, June 30). *Micro-SPECT Projects*. Available: http://www.gla.ac.uk/departments/glasgowexperimentalmricentre/micro-spectprojects/

[27] Imaging Techology. (2010, June 30). *Micro SPECT/CT*. Available: http://www.itnonline.net/files/imagecache/100-wide/U-SPECT-CT+copy.jpg

[28] Dewaraja Y. K., *Accuracy of 131I Tumor Quantification in Radioimmunotherapy Using SPECT Imaging with an Ultra-High-Energy Collimator: Monte Carlo Study*, J. Nucl. Med, vol. 46, pp. 840-849, 2005.

[29] Knesaurek K., et. al., *Comparison of correction techniques for simultaneous 201Tl/99mTc myocardial perfusion SPECT imaging: a dog study*, Phys Med Biol, vol. 45, pp. N167-76, 2000.

[30] Stabin M. G.. (2010, July 27). *Doses from Medical Radiation Sources*. Available: http://www.hps.org/hpspublications/articles/dosesfrommedicalradiation.html

[31] Stanford Dosimetry LLC. *RADAR Medical Procedure Radiation Dose Calculator*. Available: http://www.doseinfo-radar.com/RADARDoseRiskCalc.html

[32] Acharya T., *Image Processing Principles and Applications*: John Wiley & Sons, 2005.

[33] Bankman I. N., *Handbook of Medical Imaging*: Academic Press, 2000.

[34] Zhen Ma, *A Review on the Current Segmentation Algorithms for Medical Images*, IMAGAPP 2009, 2009.

[35] Wang Y., et. al., *Medical Image Segmentation Based on Deformable Models and Its Applications*, Deformable Models: Theory and Biomaterial Applications. Chapter 7, Springer-Verlag, pp. 209-260, 2007.

[36] Sun X., et al., *3D computerized segmentation of lung volume with computed tomography*, Acad Radiol, vol. 13, pp. 670-7, 2006.

[37] Leia C., et. al., *Automated lung segmentation algorithm for CAD system of thoracic CT*, Journal of Medical Colleges of PLA, vol. 23, pp. 215-222, 2008.

[38] Zhou X., et al., *Automatic segmentation and recognition of anatomical lung structures from high-resolution chest CT images*, Comput Med Imaging Graph, vol. 30, pp. 299-313, 2006.

[39] Pu J., et al., *Adaptive border marching algorithm: automatic lung segmentation on chest CT images*, Comput Med Imaging Graph, vol. 32, pp. 452-62, 2008.

[40] Kakar M., et. al., *Automatic segmentation and recognition of lungs and lesion from CT scans of thorax*, Comput Med Imaging Graph, vol. 33, pp. 72-82, 2009.

[41] He Y., *Perfusion-Ventilation Lung SPECT Image Analysis System Based on Minimum Cross-Entropy Threshold and Watershed Segmentation*, IEEE Computer Society pp. 280-284, 2008.

[42] Takenaka D., et al., *Co-registered perfusion SPECT/CT: utility for prediction of improved postoperative outcome in lung volume reduction surgery candidates*, Eur J Radiol, vol. 74, pp. 465-72, 2010.

[43] Suga K., et al., *Functional mechanism of lung mosaic CT attenuation: assessment with deep-inspiration breath-hold perfusion SPECT-CT fusion imaging and non-breath-hold Technegas SPECT*, Acta Radiol, vol. 50, pp. 34-41, 2009.

[44] Palmer J., et al., *Comprehensive ventilation/perfusion SPECT*, J Nucl Med, vol. 42, pp. 1288-94, 2001.

[45] Hajnal J. V., et. al., *Medical Image Registration*, CRC Press, 2001.

[46] Crum W. R., et al., *Non-rigid image registration: theory and practice*, Br J Radiol, vol. 77 Spec No 2, pp. S140-53, 2004.

[47] Woo J., et. al., *Automated multi-modality registration of 64-slice coronary CT angiography with myocardial perfusion SPECT*, Biomedical Imaging: From Nano to Macro, 2009. ISBI '09. IEEE International Symposium, pp. 358 - 361, 2009.

[48] Song J., et al., *A hybrid optimization model based on multi-metrics for registration using free-form deformation*, Conf Proc IEEE Eng Med Biol Soc, vol. 2007, pp. 6392-5, 2007.

[49] Pan Y., et. al., *Estimation of regional lung expansion via 3D image registration*, Proc. SPIE 2005, pp. 453–464, 2005.

[50] Hahn D. A., et.al., *A practical salient region feature based 3D multi-modality registration method for medical images*, Medical Imaging 2006: Image Processing, vol. 6144, pp. 870-879, 2006.

[51] Yin L., et al., *Quantitative evaluation on the accuracy of image registration methods in SPECT guided radiation therapy for lung cancer patients*, Canadian Organization of Medical Physicists 55th Annual Scientific Meeting (COMP 2009), 2009.

[52] Papp L., et. al., *Extended Normalized Mutual Information for Lung SPECT - CT Registration*, Bioinformatics and Biomedical Engineering , 2009. ICBBE 2009. 3rd International Conference, pp. 1 - 3, 2009.

[53] Center For Information Techology, *Medical Image Processing, Analysis and Visualization (MIPAV)*, v. 4.4.1 (2010-02-19), 2010.

[54] Vercauteren T., et al., *Diffeomorphic demons: efficient non-parametric image registration*, Neuroimage, vol. 45, pp. S61-72, 2009.

[55] Kalender W. A., *Computed tomography: fundamentals, system technology, image quality, applications*, Publicis MCD Verlag, 2000.

[56] Isidoro J., et. al., *A Processing and Review Program for Lung Pulmonary Embolism SPECT studies*, Eur. J. Nucl. Med. Mol. Imaging, vol. 32, 2009.

[57] Vercauteren T., et al., *Symmetric log-domain diffeomorphic Registration: a demons-based approach*, Med Image Comput Comput Assist Interv, vol. 11, pp. 754-61, 2008.

[58] Mathews J. H., (2010, June 15), *Powell Algorithm*. Available: http://math.fullerton.edu/mathews/n2003/PowellMethodMod.html

[59] MathWorks, *Image Processing Toolbox v6.3 For use with MATLAB 7.8*,, ed: The MathWorks Inc., 2009.

[60] Myronenko A., *Rview*, v. 8.218 Beta, 2010.

[61] (2010, August 30). *Anatomy Tutorial: Anatomic Position*. Available: http://www.vhlab.umn.edu/atlas/anatutorial/anatutorial1.shtml

[62] NetMBA Business Knowledge Center. (2010, August 30). *Box Plots*. Available: http://www.netmba.com/statistics/plot/box/

[63] MathWorks, *Statistics Toolbox For use with MATLAB*, ed, 2009.